A micro-scale inspired chemo-mechanical model of bonded geomaterials

Alessandro Gajo[1], Francesco Cecinato[1,*], Tomasz Hueckel[2]

[1]University of Trento, Department of Civil, Environmental and Mechanical Engineering, Trento, Italy.

[2]Duke University, Civil and Environmental Engineering, Durham, NC, USA.

[*]Corresponding author. Email: francesco.cecinato@unitn.it

Abstract

Chemical processes influence the mechanical properties of geomaterials, resulting in either strengthening or weakening effects, the latter being particularly critical for long-term safety assessment in civil and energy engineering. Coupling of chemical and mechanical processes in cemented soils and rocks is investigated starting form a micro-structural chemo-mechanical model. The model consists of an assembly of grains and bonds undergoing dissolution or precipitation of mineral mass, affecting geometrical characteristics of the assembly. The principal such characteristics are the evolution of specific surface area and of bond cross-sectional area at the micro-scale, and of porosity at the macro-scale, which become key variables linking the micro-scale and macro-scale mechanisms. This framework has the advantage of avoiding unphysical situations, such as the occurrence of mineral precipitation with no pore space available or the occurrence of dissolution with no cementing material left. The evolution of important micromechanical quantities, such as the number of active bonds and their cross section is tracked. At the macro-scale, a reactive chemo-plasticity model is combined with a model for bonded geomaterials. The resulting micro- to macro-scale transition, schematically applicable to both materials with reactive grains and bonds and materials with only reacting bonds, is validated against the available experimental evidence, concerning calcarenite with both reactive bonds and grains made of the same mineral. The model is thus shown to provide a flexible framework for a consistent interpretation of experimental loading paths, and can be readily extended to more complex circumstances.

1. Introduction

Terzaghi [1] in his paper on Mechanism of Landslide discusses "landslide producing processes" where he distinguishes between "causes" and "contributing factors" of landslides. In particular, he states, "if a slope is old, heavy rainstorms (…) can hardly be the sole cause of a slope failure, because it is most unlikely that they are without any precedent in the history of the slope. They can only be considered contributing

factors". Further ahead, in Table 1, among several "modes of action of agent" linked to water as the "acting agent" from heavy rain or snow melt, Terzaghi lists at # 9 the chemical weathering which "weakens intergranular bonds" leading to decrease in cohesion. For "old slopes", he then shows a progressive decrease in Factor of Safety, over 15 years, with some local ups and downs corresponding to dry and wet spells, reaching 1, in conjunction with "a contributing factor" of high pore water pressure. He returns to this mechanism in the case of loess, where water from external reservoirs is listed as removing soluble binders destroying intergranular bond(s), with the same macroscopic effect of a decreasing cohesion.

Sensitivity of basic mechanical soil properties to chemical processes in the environment has been seen to become a critical factor of stability of slopes and coastal structures for a variety of reasons, from periodic changes in salinity of pore water affecting clay behavior of coastal slopes [2], [3] to oxidation and dissolution of sandstone [4], to dissolution of calcite [5], dissolution of silica in aging sediments [6], dissolution of gypsum in abandoned mines [7], to mention just a few examples.

In a more modern day context one needs to add that the dissolution of cementation bonds indicated by [1] may be dramatically enhanced and accelerated by an increase in acidity of the run-off water, namely from an acid rain. In a case study of two landslide slip surfaces at Diao Jiao Zui and Qian Jiang Ping sites in the Three Gorges area, China, geochemical testing revealed that due to acid rain (with pH between 5.4 and 3.45) potassium ions at the slide surface were released, the cementation was reduced, and the ratio of interlayer clay minerals evolved. Accordingly, illite or montmorillonite-illite mixtures were transformed into montmorillonite associated with a strength change, including a 30% drop in shear strength [8].

Further, the recent interest in geological CO_2 sequestration in carbonate rocks brings challenges in predicting the effectiveness of the process, since the injected CO_2 dissolves into an in-situ brine and produces also a weak acid, which in turn reacts with the surrounding carbonate rock (e.g. see [9], [10]). On the other hand, the technique of acid softening of rocks prior to hydraulic fracturing in unconventional gas and oil recovery or heat recovery from geothermal reservoirs poses interesting questions in ensuring the control of the process [11].

The aim of this paper is to investigate a coupling of chemical and mechanical processes involved in weakening or strengthening of bonded geomaterials by means of a micro-structure inspired model. The micro-scale model is calibrated on (but it is not limited to) a regular array of grains and bonds undergoing dissolution or deposition of mineral mass. Only reactions of dissolution and precipitation between pore fluid and solid minerals are considered for the moment, neglecting complex phenomena involving solid-solid mass exchange (between bonds and grains, or between different sized minerals like in the Ostwald ripening phenomenon, cf. [12]). Rate equations for mineral dissolution and precipitation are considered as known [13], [14]. Variable geometrical characteristics of the micro-structure are used to determine the evolving specific surface area (see [15], [16]) and the bond resisting cross-sectional area at the micro-scale,

and variable porosity at the macro-scale, which become key variables linking the micro-scale and macro-scale mechanisms. At the macro-scale, a reactive chemo-plasticity model [17], [18] is combined with a model for bonded geomaterials [19], [20] and [21].

Based on the kinetics of dissolution/deposition reaction of different minerals, two limiting cases can be considered, namely the case of both reactive grains and reactive bonds (e.g. calcarenite, where both grains and bonds are made of calcium carbonate) and the case of non-reactive grains and reactive bonds (e.g. silicic sand with carbonate bonds). While in the former case the timescales of dissolution/deposition of grains and bonds are comparable, in the latter case the timescale of reaction of the grains is orders of magnitude larger compared to that of bonds. In this work, due to the wide availability of relevant experimental evidence for validation, emphasis is put on the case of both reactive grains and bonds. However, the proposed framework could be easily extended to other cases, e.g. situations involving the presence of different families of cementation bonds characterized by different strengths and chemical dissolution properties.

The framework presented here aims at realistically reproducing the changes in the microscopic geometry of saturated bonded geomaterials due to both chemical dissolution/deposition and mechanical degradation, and consistently using them to quantify the macroscopic chemo-mechanical behavior of the material. This approach has the advantage of naturally providing the two limits of null dissolution (when cementing mineral is completely depleted) and null precipitation (when the porosity is null). The presented framework is not specialized for a particular geomaterial but aims at being more wide-ranging than existing works, and can be suited to different material types and modeling needs upon modifying key parameters.

Two types of data can be obtained using the existing technologies: data on the material strength change (decline) and on stiffness change, due to both the mechanical loading and chemical dissolution - that is typically provided by macro-scale experiments; and data about the chemical processes of dissolution and precipitation of the key minerals, which is obtained from micro-scale observation. Consequently, we are in the position to construct a two-scale model, which includes: (i) a macro-scale chemo-elasto-plastic model, where both the apparent preconsolidation stress and the apparent isotropic tensile strength depend on the material microstructural features, and (ii) an integrated model for mass change of minerals, in the framework of an evolving idealized micro-scale structure of grains and bonds, subject also to mechanical failure and chemical healing.

An example of a 2D material micro-scale structure is sketched in Figure 1, inspired by micrographs of thin sections of calcarenite (e.g. see [31]), showing a gradual loss of mass and the consequent porosity increase due to chemical dissolution of both grains and bonds.

A constitutive model for the mechanical behavior of a reactive geomaterial that makes explicit use of a

kinetic equation of a chemical reaction for a mineral, needs to be associated with a volume fraction of such mineral within a unit volume of soil. In the considered case it is assumed that bonds can be clearly identified at the micro-structure, and are made of a single mineral. The macro-scale is described by continuum variables of (elastic and plastic) strain and stress tensors, porosity, continuum free energy, and compressive and tensile strength. Such variables all depend on a series of macro-scale variables, such as the mass change of the minerals, and on micro-structural variables, as the geometry of bonds and grains, through phenomenological cross-scale functions, or averaging, or homogenization procedures.

In Section 2, the key literature evidence about chemo-mechanical coupling is discussed, both from the experimental and the constitutive modeling point of view. In Section 3 the macro-scale model is outlined, in terms of the key elasto-plastic features and of the macroscopic rate equations, defining the couplings between the mechanical and chemical behavior of the material. Section 4 is devoted to describing the derivation and calibration of cross-scale functions, enabling us to perform chemo-mechanical macroscale calculations accounting for the microstructure, while in Section 5 guidance is provided in the selection of constitutive parameters and initial values, with emphasis on the newly introduced variables compared to existing models. Finally, in Section 6 the model is validated by simulating a number of experimental chemo-mechanical loading paths reported in the literature, and conclusions are drawn in Section 7.

2.   Phenomenological and modeling background

A common mechanism of chemical weakening or strengthening of soil is related to dissolution or precipitation of minerals, mainly calcium carbonate or silicates from and into intergranular bonds. In particular, dissolution of intergranular bonds as a result of water inundation, often in concomitance with dissolution or transformation of illite into smectite, or in the presence of highly acidic water, are considered as particularly adverse conditions. This is especially because little attention is paid to geochemical aspects of soil's mechanical evolution [1], [22] and [23]. Intergranular bonds often constitute a crucial and critical element of the so-called peak (undisturbed) material strength reached through shear or tensile loading, subject to axial or isotropic stress states, and possible drop of strength as a result of what is known as destructuration. In terms of micro-structural evolution, this may mean the rupture of certain populations of bonds, under a class of stress modes. Debonding is interpreted as a progressive failure of individual bonds, so that the overall process after its inception is relatively smooth. Debonding processes also affect elastic material properties. Because of bond breaking, the overall elasticity may be significantly reduced in shear, while the bulk (isotropic) modulus (in compaction) may be either increased or decreased. Viewed as a dependence of macroscopic elasticity on the amount of plastic deformation from the stand point of elasto-plasticity, this amounts to elasto-plastic coupling [24], [25] or if the process induces elastic anisotropy, to plasticity dependent elastic anisotropy [26], [27], [28] and [29].

There is a relatively modest collection of data reported on the loss of strength at the macro-scale

because of dissolution of key minerals. Castellanza and Nova [30] report oedometer test results demonstrating changes in apparent preconsolidation pressure upon exposure to a weak acid solution (pH = 2.8) both in calcarenite and in an artificial material made of silica sand bonded by lime. Remarkably, they measured a gradual, asymptotic decrease of apparent preconsolidation stress in calcarenite up to 70% of the original strength, increasing with the time of exposure to acid (cf. Fig. 12 of [30]). For the same group of calcarenites, Ciantia et al. [31] found a drop in uniaxial compressive strength of the order of one fourth to one third, upon wetting by respectively water and water with acid (with pH between 3.75 and 2.25). In the same experiments, a tensile strength reduction is also observed in water-inundated specimens of up to 26%. Notably, also Young's modulus is observed to decline by up to 60%.

Experimental data are also available about the loss of strength of bonded geomaterials due to destructuration, i.e. bond breakage due to mechanical loading. In this context, a significant set of results is reported in [36], where the behavior of calcarenite under isotropic and triaxial loading paths is explored. All tests show the occurrence of a well-defined destructuration phase during loading, in which the material undergoes transition from rock-like to soil-like material at constant stress. Lagioia and Nova [36] also lay the foundations of a mathematical model for bonded materials that has subsequently seen further developments by the same group of authors.

From the constitutive modeling point of view, the mechanics of bonded geomaterials have been investigated through an extended version of the Cam Clay model (e.g. [19], [36] and [21]), in which a plastic strain dependent isotropic tensile strength function is included, either coupled or decoupled from the classical preconsolidation hardening function. Bonded materials are often viewed as materials in a "natural state" with a structure, as opposed to materials in a "destructured" or "remolded" state. The latter state is reached via a process of destructuration, which is characterized by a gradual (as opposed to brittle) loss of strength, both in terms of isotropic tensile strength and shear strength as a result (and thus as a phenomenological function) of plastic straining. These mechanisms are conceived in the frame of Cam-clay plasticity and/or bounding surface plasticity [37], [38] and [39]. However, the above cited works are purely macroscopic, and apply to chemically inert environments. Coupled chemo-plasticity models have been developed either as a single scale or multi- scale models. Principles of single-scale models, formulated at the macroscale, are discussed in [40], [17], [18] and [41], with focus on the chemo-hydro-mechanical behavior of saturated clay materials. Hu and Hueckel [11] proposed a three-scale model for granular materials linking irreversible damage strain with associated generation of micro-cracks to mineral dissolution, from the individual grain level to the meso-scale (an aggregation of a few grains) to the macro-scale representing a large assembly of grains. Ciantia and Hueckel [5] further built up on this three-scale concept, developing a model for the long-term weathering processes in calcarenite rocks, calibrated by reproducing compression tests in samples exposed to different degrees of acid weathering.

1 **3. Macro-scale model**

2 **3.1 Yield function and hardening law**

3   The macroscopic constitutive model is developed assuming that the material behavior is isotropic,

4 undergoing small strains, and the solid constituents are assumed incompressible. Only the features of the

5 model that differ significantly from the standard critical state framework (e.g., [42]) are presented

6 hereafter. The yield function is proposed along the lines of an existing approach for bonded geomaterials

7 (e.g. [19], [20] and [21]), in which an isotropic tensile strength function is included, as an extension of the

8 modified Cam Clay model [43]. The expression of the yield locus written in generalized stress space

9 (compression is here taken positive) is

10
$$\mathcal{F}\left(\boldsymbol{\sigma},\boldsymbol{\varepsilon}_p,a_b\right)=\left[M_{cv}L\left(\theta\right)\right]^2\left[\left(p+p_{tens}\right)^2-\left(p+p_{tens}\right)\left(p_c+p_{comp}+p_{tens}\right)\right]+q^2 \tag{1}$$

11 where M_{cv} is the critical state (i.e., constant volume) parameter, $L\left(\theta\right)$ is a function of the Lode angle

12 describing the deviatoric section of the yield surface (in this work the function proposed by Willam &

13 Warnke [44], has been used) , $p=I_\sigma/3$ is the mean effective pressure, where I_σ the first invariant of the

14 effective stress tensor $\boldsymbol{\sigma}$ (note that the usual prime is omitted for brevity), $q=\sqrt{3J_{2\sigma}}$ the deviatoric

15 stress, where $J_{2\sigma}$ the second invariant of the deviatoric part of $\boldsymbol{\sigma}$ (e.g. see [45]), and p_c is the (positive)

16 preconsolidation pressure of the uncemented soil. The two positive macroscopic quantities p_{tens} and p_{comp}

17 respectively represent the increase of tensile and compressive strength, compared to uncemented soil, due

18 to the presence of cementation bonds. Coupling with the micromechanical behavior is introduced here, by

19 assuming that

20
$$p_{tens}=a_b\sigma_{rt} \quad \text{and} \quad p_{comp}=a_b\sigma_{rc} \tag{2}$$

21 where σ_{rt} and σ_{rc} are the macroscopic tensile and compressive strength (or the Euler stability stress, if

22 Euler stability of bonds is taken into account) of the material constituting the cementing bonds, while a_b is

23 the mean specific cross section area of all mechanically active cementing bonds (corresponding to

24 unbroken bonds). The macroscopic variable a_b (with units m^2/m^2) depends on microscale quantities

25 through an important cross-scale function discussed in detail in Section 4.1, and represents the total area

26 of bonds in the porous skeleton's cross section per unit cross sectional area, only accounting for those

27 bonds that are not broken, thus 'actively' contributing to the macroscopic strength.

28   It should be noted that when the material is completely destructed (i.e., with no active cementation

29 bonds left), $a_b=0$, thus $p_{tens}=0$ and $p_{comp}=0$, hence the modified Cam Clay yield locus is recovered

30 from equation (1). In Figure 2 the evolution of the yield surface with cementation/destructuration is shown

1   in terms of invariants (p, q). It should be observed that the line of slope M_{cv} (assumed independent of

2   chemical effects for the sake of simplicity), passing by the yield locus' horizontal tangent point, actually

3   identifies critical state only in the uncemented soil configuration, whereas in all other cases it represents a

4   stress state at nil plastic volumetric strain rate, while the size of the yield locus can continue to evolve.

5   It is assumed that the yield surface crosses the isotropic stress axis in the zone of tension (negative value

6   of mean pressure) at $-p_{tens}$ and in compression (positive values of mean pressure) at $(p_c + p_{comp})$, cf.

7   Figure 2, where the macroscopic preconsolidation pressure p_c can be expressed as

$$p_c = p_0 \exp\left\{\frac{1+e_0}{\lambda}\left[\varepsilon_p^v - \varepsilon_0\right]\right\}, \tag{3}$$

9   where p_0, ε_0 and e_0 are the reference mean pressure, volumetric strain and void ratio respectively, ε_p^v is

10 the plastic volumetric strain and λ is a constitutive parameter. Equation (3) provides a simplified hardening

11 relationship similar to that of Cam Clay, which has been simplified by assuming negligible elastic

12 compressibility. However, the proposed constitutive framework is not limited to such simple assumptions.

13 The preconsolidation pressure defined in equation (3) is representative of the hardening state of the

14 material in its unbonded condition, and directly depends on the accumulated volumetric plastic strain ε_p^v.

15 In addition, the coupling with micromechanical behavior introduced with equations (2) implies the

16 dependence of both macroscopic functions p_{tens} and p_{comp} on the number of mechanically active bonds,

17 whose rate of change is bound to depend on both plastic straining (mechanical macro-scale effect) and on

18 mass deposition/dissolution (chemical micro-scale effects), as shown in Section 4.1 (eqn. (7)).

3.2 Elastic behavior

20   The macroscopic strain tensor is decomposed into additive elastic and plastic parts. The macroscopic

21 elastic behavior of the material is described in the framework of hyperelasticity and elasto-plastic coupling

22 [24], [25], and can thus be deduced upon defining a suitable elastic free energy density function. To

23 account for the presence of both mechanically and chemically interacting bonds and grains, the standard

24 linear elasticity form of the free energy function of the uncemented solid skeleton (i.e. the unbonded soil)

25 $\varphi_g = \varphi_g(\mathbf{\varepsilon}_e)$ is modified, based on phenomenological interpretations, into a more general function:

$$\varphi = \varphi\left(\mathbf{\varepsilon}_e, \mathbf{\varepsilon}_p, m_b, m_g\right). \tag{4}$$

27   Macroscopic variables m_b and m_g (expressed by the cross-scale functions introduced in Section 4.1)

28 are the time-integrated mass change of all mechanically active cementing bonds and of grains, respectively,

per unit volume, from a reference configuration m_{b0}, m_{g0} ($\Delta m_b, \Delta m_g > 0$ implies an increase of solid mass with respect to the reference configuration). For the sake of simplicity, since the model will be validated against chemo-mechanical degradation experiments (Section 6), a detailed description is provided here only for chemo-mechanical elastic weakening of the material, i.e. only the role of mechanical destructuration and chemical dissolution effects in the material elastic behavior are described. The more complex effects of chemical deposition, causing elastic strengthening, can be represented by a step-wise function that is not discussed in this work, for the sake of brevity.

We postulate that the macroscopic elastic free energy for a material with both reacting grains and bonds is expressed by

$$\varphi\left(\mathbf{\varepsilon}_e, \mathbf{\varepsilon}_p, m_b, m_g\right) = (1 - \tilde{\omega})\ \varphi_g\left(\mathbf{\varepsilon}_e - \frac{\left\langle -\Delta m_g \right\rangle}{\rho_s}\mathbf{I}\right) + \tilde{\omega}\ \varphi_b\left(\mathbf{\varepsilon}_e\right) \tag{5}$$

where φ_g is the free energy of the uncemented solid skeleton, φ_b is the free energy of the completely cemented soil (implying a larger stiffness than that of the unbonded material, since the whole porous space is filled with cement), $\mathbf{I}$ is the second order identity tensor, $\Delta m_g = m_g - m_{g0}$ the current change of specific mass of grains, m_g, with respect to the initial value m_{g0}. The weighting function $0 \le \tilde{\omega} \le 1$ is set to be a function of the value of the mean specific cross section area of mechanically active bonds a_b (that depends on both cement mass change and plastic strain), as $\tilde{\omega} = a_b{}^\alpha$, where α is a positive constitutive parameter. In this way, both elasto-plastic and chemical couplings are taken into account. Note that Macaulay brackets $\left\langle -\Delta m_b \right\rangle$ are used because macroscopic volume strains are induced by chemo-mechanical coupling only in the case of grain dissolution (and not of cement deposition).

Notably, eqn. (5) accounts for the occurrence of some macroscopic volumetric strain induced by grain dissolution. In fact, in the limit of null active cementing bonds (i.e. for small values of $\tilde{\omega}$), grain dissolution is associated to volume compression (due to the decrease of grain volume). The volumetric effect of grain dissolution in uncemented soil is completely analogous to the volumetric effect of a decrease of temperature in the grain material, in contrast with the effect of deposition, which is assumed to produce no volumetric strain. It should be however remarked that macroscopic volume strains induced by chemical dissolution are expected to be important only in the case of small volume of active bonds (i.e., when $\tilde{\omega}$ is small).

In addition to, and enhanced by the chemical degradation, the structure of the material may suffer from a mechanically induced destructuration. This is measured by plastic strain and brings about a reduction of the number of mechanically active bonds, resulting in the reduction of a_b, mean specific cross section area

1 of mechanically active bonds, and hence of $\tilde{\omega} = a_b{}^{\alpha}$. As a result, the first term of expression (5),

2 representing the elastic energy of the destructured material (i.e. without any bonds), will gain larger

3 relative importance, thus the overall material stiffness will decrease. When by subsequent chemo-

4 mechanical evolution all the active cement bonds are broken $a_b = 0$, then the free energy of the

5 uncemented solid skeleton φ_g is recovered. Whereas, when the porous material is completely cemented,

6 $a_b \to 1$, the free energy becomes that of completely cemented soil φ_b.

7   From the chemical point of view, during cement dissolution a fraction of cement bonds, which in a

8 general situation carries a fraction of the overall stress, disappears, causing the reduction of a_b. This leads

9 to a stress increase in the remaining fractions of the bonds, thus inducing strains at constant stress level. As

10 a result, cement dissolution induces a decrease of soil stiffness with associated strains (if dissolution occurs

11 at constant stress) or a decrease of soil stiffness with an associated decrease of applied stress (if dissolution

12 occurs at constant strain). These effects are adequately represented by eqn. (5).

13   It should be finally remarked that in eqn. (5) the compressibility of the solid constituents has been

14 neglected. Further, only stiffness degradation due to bond breakage is considered in eqn. (5), while the

15 increase of stiffness due to compaction is neglected for simplicity. The latter would imply a dependence of

16 φ_g on the porosity of solid skeleton, without including the volumes of the bonds.

17   **3.3 Macroscopic chemo-mechanical rate equations**

18   From the macroscopic point of view, the net mass change $\dot{m}$ within the REV due to dissolution and/or

19 deposition is controlled by chemical kinetics. The rate of these reactions is proportional to the specific

20 reactive surface area a_r (with units m²/m³) per unit volume of the reacting materials, which corresponds to

21 the area per unit volume of all interfaces of the porous skeleton that are exposed to chemical interaction,

22 i.e. the areas of bonds and grains that are actually in contact with the pore fluid, and is defined by another

23 important cross-scale function (Section 4.1).

24   Once the specific reactive surface area has been determined (see Section 4), the chemical reaction rate

25 can be generally described by the following kinetic equation for the rate of mass change (i.e. specific mass

26 change per unit time) of a specific mineral "i" (see e.g. [48])

27
$$\dot{m}^i = a_r^i k^i \left(\mu^i{}_s - \mu_f \right) \tag{6}$$

28 with k^i a rate constant (with units (kg mol)/(m² s J)), a_r^i the specific surface area of each mineral (with

29 units m²/m³), and $\mu^i{}_s$ and μ_f the chemical potentials (with units of J/mol) of the reacting solid mineral "i"

1   and of the fluid respectively. The rate constants k^i are well established for most minerals (see e.g. [49]).

2   For the sake of simplicity, a single reacting mineral will be considered both in the bonds and in the grains.

3   It can be observed that upon mass changes, also the specific reactive surface area in general changes,

4   due to the evolving geometry of the solids. Thus, at constant chemical potential difference (e.g. if in an

5   open system the material is subject to flushing with an acid solution), the mass rate of change evolves with

6   the microscopic geometry of the system, which is represented by a_r. It should be also remarked that open

7   systems only are considered in this work, for the sake of simplicity, implying that the dissolved mineral

8   mass is transported away by the pore fluid (by advection-diffusion) and thus no saturation of the pore fluid

9   solution is considered. Modelling the transport of species within and outside the REV is out of the scope of

10   the present work.

11   Let us denote with N_b (with dimensions of $1/L^3$) the number of potential (i.e. broken and unbroken)

12   bonds per unit volume of the porous skeleton. It should be remarked that not all bonds within the REV are

13   mechanically active, due for instance to (partial) bond rupture consequent to mechanical loading. In fact,

14   only the unbroken bonds will contribute to the macroscopic strength and stiffness of the material. Hence,

15   we define the macroscopic quantity N_{ba} as the number of mechanically active bonds per unit volume. N_{ba}

16   ranges between 0 and N_b (i.e. $0 \leq N_{ba} \leq N_b$) with $N_{ba} = 0$ when all bonds are broken, and $N_{ba} = N_b$ when

17   no bond is broken. The quantity N_{ba} depends both on the amount of bond ruptures induced by mechanical

18   loading (i.e., destructuration) and on the deposition of cement at broken bonds (with the consequent

19   curing of broken bonds). The following empirical cross-scale function is proposed for the rate of N_{ba}, in

20   which the two mechanisms of destructuration and cement deposition are clearly distinguishable:

21
$$\dot{N}_{ba} = -k_1 N_{ba} \sqrt{(1-A)(\dot{\varepsilon}_p^v)^2 + A(\dot{\varepsilon}_p^s)^2} + k_2 (N_b - N_{ba})\langle \dot{m}_b \rangle \qquad (7)$$

22   In the above, A, k_1 (dimensionless) and k_2 (with units m^3/kg) are constitutive parameters, with A

23   ranging between 0 and 1 and weighting the role of volumetric ($\dot{\varepsilon}_p^v$) and deviatoric ($\dot{\varepsilon}_p^s$) plastic strain rates

24   in destructuration (i.e., decementation). The deviatoric plastic strain rate is defined as $\dot{\varepsilon}_p^s = \sqrt{(2/3)J_{2\varepsilon}}$,

25   where $J_{2\varepsilon}$ the second invariant of the increment of the plastic deviatoric strain tensor (e.g. see [45]). The

26   Macaulay brackets in the last term of eqn. (7) are needed because only cement deposition is assumed to

27   form new active bonds, whereas plastic strains are assumed to induce only bond rupture. Positive $\dot{m}_b$ is

28   associated with mass increase (due to deposition) of bonds.

1   As a result, in general cement dissolution/deposition $\dot{m}_b$ affects soil's mechanical strength in two ways,

2   namely (i) through the restoration of previously broken bonds (with an increase of the number of active

3   bonds N_{ba}, second term of eqn. 7) and (ii) through the reduction/increase of the bond cross sections. In

4   fact, in general cement dissolution/deposition $\dot{m} = \dot{m}_g + \dot{m}_b$ is expected to affect both porosity and the

5   thickness of bonds. Thus, it is reasonable to assume that the fractions of $\dot{m} = \dot{m}_g + \dot{m}_b$ involving grains and

6   bonds are proportional to the respective reactive specific surface areas a_{rg} and a_{rb}, namely

$$\dot{m}_b = \frac{a_{rb}}{a_{rb} + a_{rg}} \dot{m} \quad \text{and} \quad \dot{m}_g = \frac{a_{rg}}{a_{rb} + a_{rg}} \dot{m} . \tag{8}$$

8   Starting from the standard definition of porosity, upon chemo-mechanical loading, the rate of porosity

9   change of the material is thus deemed to depend on both mass change and on volumetric strain, as follows:

$$\dot{n} = -\frac{\dot{m}}{\rho_s} - (1 - n) Tr(\dot{\boldsymbol{\varepsilon}}) . \tag{9}$$

11   The above represents the equation of continuity for the porous skeleton (due to the assumption of

12   incompressible solid constituents). Within the proposed chemo-mechanical framework based on small

13   strains concepts, it is convenient to introduce here a 'small strain' porosity $\tilde{n}$ depending only on mass

14   dissolution/deposition and neglecting volumetric strain, through the following rate equation:

$$\dot{\tilde{n}} = -\frac{\dot{m}}{\rho_s} . \tag{10}$$

16   It should be remarked that $\dot{\tilde{n}}$ is simply a fraction of $\dot{n}$, thus $\tilde{n}$ and n are not referred to different

17   spatial configurations.

18   **4.   Microscale description and micro-to-macro relationships**

19   In this section the cross-scale functions defining key macroscopic variables a_b and a_r, enabling us to

20   perform chemo-mechanical macroscopic calculations accounting for the microstructure, are derived in

21   terms of microscopic variables, with reference to a simplified microscopic geometry. Cross-scale functions

22   are then calibrated based on a rigorous microscopic geometry calculation assuming a cubical representative

23   elementary volume (REV) as an example. However, these interpolation functions can be easily adapted to

24   different micromechanical models.

25   In Figure 3, a 2D idealization of the considered geometry at the microscopic scale (where the key

26   dimensions of grains and bonds are indicated) inspired from the realistic schemes of Figure 1 is shown, in

the general case where grains might not be in direct contact, but they are linked by cementation bonds that are assumed to be isotropically distributed. In a large porosity configuration such as that illustrated in Figure 3, the geometry of bonds can be approximated with that of a cylinder, and the geometry of grains can be represented by that of a sphere. This geometry is assumed to represent the reference configuration for materials where both grains and bonds are subject to the same rate of dissolution/deposition. In fact, it can be expected that at a generic instant of the dissolution/deposition history of such materials the grains appear linked by cement bonds but are not necessarily in direct contact (Figure 1 and Figure 3).

4.1 Derivation of cross-scale functions

Let us denote with N_g (with dimensions of 1/L³) the number of grains per unit initial bulk volume of the porous skeleton. With reference to the general case of Figure 3, let R_g be the mean radius of the grains, R_b the mean radius of the bonds, and L_b the mean length of the bonds, which is generally defined as $L_b = d + 2h$, where $d \neq 0$ the distance between the edges of two grains connected by a bond, and h the height of the spherical sector wrapped by the bond, which is expressed as

$$h = R_g - \sqrt{R_g^2 - R_b^2} \ . \tag{11}$$

According to the above introduced notation, we can easily deduce the specific volume of the grains $v_g = N_g \dfrac{4}{3} \pi R_g^3$ (expressed as L³/L³ and referred to the unit initial bulk volume) and that of the bonds (volume of the cylinders less the volume of spherical sectors wrapped by the bonds) as

$$v_b = N_b \pi \left[R_b L_b^2 - h \left(R_b^2 + h^2 / 3 \right) \right]. \tag{12}$$

Thus, the volume of the solid phase (per unit initial volume of the porous skeleton) coincides with

$$1 - \tilde{n} = v_b + v_g \tag{13}$$

where $\tilde{n}$ the 'small strain' porosity (eqn. (10)), whereas the solid masses of the grains and of the bonds can be easily deduced by multiplying the specific volumes by the density of solids ρ_s.

The specific reactive surface area a_r (per unit bulk volume, expressed in L²/L³) can be expressed as the sum of the specific area of grains and of bonds. The latter coincides with the sum of the lateral surface area of all the bonds and of the cross section areas of the broken bonds (which are N_b - N_{ba}), and is equal to

$$a_{rb} = N_b 2\pi R_b L_b + \left(N_b - N_{ba} \right) \pi R_b^2 \tag{14}$$

whereas the reactive specific surface area of the grains is given by

$$a_{rg} = N_g \, 4\pi R_g^2 - N_b \, 2\pi R_b h \, . \tag{15}$$

Thus, the specific reactive surface area (of grains and bonds) is

$$a_r = a_{rg} + a_{rb} = N_g \, 4\pi R_g^2 - N_b \, 2\pi R_b h + N_b \pi R_b L_b + \left(N_b - N_{ba} \right) \pi R_b^2 \, . \tag{16}$$

It should be observed that the expressions of specific reactive surface area given above are valid as long as the porosity is large, as exemplified in Figure 1 and Figure 3, because, when the volume of bonds and of grains is large (and the porosity becomes negligible), the reactive surface area is expected to become negligible. Indeed, at the end-phase of precipitation, when the volumes of growing neighboring bonds and grains start to overlap, details of the geometry of bonds become very intricate.

Hence, to relate the microstructure to the macroscopic behavior, instead of strictly following a given microscopic geometry, we introduce phenomenological restrictions to avoid physical inconsistencies in the system evolution. In particular, when the volume of precipitates fills all the available voids space, $n \to 0$ is enforced; and when all bonds are dissolved, i.e. $n \to 1$, the specific reactive surface area a_r is imposed to tend to zero. When porosity tends to zero, a general asymptotic relationship between and a_r and n holds:

$$a_r = a_{r0} n^\gamma \tag{17}$$

where a_{r0} and the exponent γ are constitutive parameters. The above can be obtained by assuming that, in the limit of very small porosity, the porous space is described by a given number of voids of given shape (e.g., spherical) per unit volume. Derivation of eqn. (17) is not illustrated in detail for the sake of brevity.

Combining eqns. (16) and (17) with an appropriate weighting function ω_1, we obtain the following relationship expressing the specific reactive surface area of materials with both reacting grains and bonds throughout the porosity range:

$$a_r = \left[N_g \, 4\pi R_g^2 - N_b \, 2\pi R_b h + N_b \, 2\pi R_b L_b + \left(N_b - N_{ba} \right) \pi R_b^2 \right] \left(1 - \omega_1^\beta \right) + a_{r0} n^\gamma \omega_1^\beta \tag{18}$$

where β is a constitutive parameter. We propose to express the weighting function ω_1 as

$$\omega_1 = 1 - n \tag{19}$$

The weighting function (19) $\omega_1 \to 0$ for $n \to 1$, and $\omega_1 \to 1$ for $n \to 0$, thus it effectively inhibits the exchange of cement mass (due to dissolution/precipitation) when there is no material left, or when there is

13

no void volume left. It is worth highlighting that, for the sake of simplicity, eqn. (18) implicitly neglects the reactive surface area due to micro-cracks that are induced at constant porosity. As a result, at vanishing porosity ($n \to 0$) $a_r \to 0$, independently of the possible existence of micro-cracks.

It should be noted that the specific reactive surface is also affected by the number of bond ruptures induced by mechanical loading. In fact, mechanical loading can induce a decrease of the number of active bonds per unit volume N_{ba} (as is discussed in Section 3.3), thus leading to an increase of reactive surface area a_r.

Moreover, the cementing bonds contribute to compressive, tensile and shear strength of the porous medium. Knowing the number of active bonds per unit volume N_{ba}, the number of active bonds per unit linear length can be expected to be of the order of $N_{ba}^{1/3}$, hence the number of active bonds per unit initial cross section of the porous skeleton (expressed in $1/L^2$) can be approximately estimated as $N_{ba}^{2/3}$. The specific cross section area of cementing bonds a_b (expressed as L^2/L^2 and referred to the unit initial cross section) can then be evaluated, at the limit of large porosity ($\tilde{n} \to 1$), as

$$a_b = \pi R_b^2 N_{ba}^{2/3} \tag{20}$$

and on the other hand, at the limit of very small porosity ($\tilde{n} \to 0$), as

$$a_b = 1 - \tilde{n} . \tag{21}$$

Applying for the specific cross section area of cementing bonds similar interpolation concepts to those adopted for the reactive specific area, we obtain

$$a_b = \pi N_{ba}^{2/3} R_b^2 \left(1 - \omega_2\right)^{\theta} \left(1 - \omega_3\right)^{\delta} + (1 - \tilde{n})\omega_2^{\theta} \omega_3^{\delta} \tag{22}$$

In the above, δ and θ are constitutive parameters, and the weighting functions ω_2 and ω_3 are proposed as

$$\omega_2 = 1 - \tilde{n} \qquad \omega_3 = \left(\frac{v_b}{1 - v_g} \right) \tag{23}$$

where (1- v_g) represents the specific volume (referred to the unit initial bulk volume) that is available for a complete cementation of bonds. Eqn. (23)b represents a function which has null value when $v_b = 0$ (no cementing bonds), and equals one when growing precipitated bonds fill all the void space, i.e. for

1     $v_b = 1 - v_g$ (no void volume). As a result, the specific cross section area of cementing bonds a_b ranges

2   between 0 (at large porosities) and 1 (at negligible porosity).

3   It is worth recalling that the use of $\tilde{n}$ (instead of n) comes from small strains theory and implies that

4   under a purely elastic deformation (with no rupture of cementation bonds and no dissolution/deposition)

5   a_b (defined in eqn. (22)) is independent of volumetric strains (as expected from a physical point of view).

6   As a result, a_b depends only on plastic strains (which can induce rupture of cementing bonds) and on

7   cement deposition/dissolution.

8   **4.2 Calibration of cross-scale functions: example representation of micro-macro relationships**

9   Since the key equations of the model outlined in Section 4.1 are not tied to a specific geometrical

10   configuration, the question arises as to how the constitutive parameters can be calibrated to represent a

11   realistic (albeit simplified) situation. To validate our constitutive assumptions, an attempt is made here to

12   describe the microscopic geometry in a rigorous manner throughout the porosity range. In other words, the

13   evolution of the geometry at the microscale due to dissolution/deposition is tracked without resorting to

14   the phenomenological simplifications described in Section 4.1. Instead, reference is made to a cubical REV

15   composed of eight spherical grains (in contact or not, with one to another), where each grain is connected

16   to six other grains by means of cylindrical bonds. The spherical grains are centered in the REV's vertices and

17   the cylindrical bond axes lie in the REV's edges, so that the porous space is located at the center of the REV.

18   The resulting trends obtained with the microscopic representation are then compared to the macroscopic

19   model representation of Section 4.1, in order to evaluate the constitutive parameters β and δ of the

20   cross-scale functions eqns. (18) and (22).

21   The reference configuration consists, as an example, of identical spherical particles that are linked by

22   identical cylindrical bonds so that the center-to center of grains distance $H_c = d + 2R_g$. No bond breakage

23   by mechanical action is considered in this example, but the geometry of the solid skeleton is changed as a

24   result of uniform deposition/dissolution, so that the gain/loss of thickness is constant per unit area,

25   throughout the solid skeleton's reacting surface.

26   The microscopic representation is subdivided into two sub-cases, corresponding to different geometrical

27   configurations occurring during chemical interaction of the material: a first configuration, at larger porosity,

28   in which both bonds and grains' surfaces are exposed to chemical interactions and thus undergo uniform

29   thickness reduction/increase. This configuration is lower-bounded by the complete dissolution of bonds

30   (when grains may spatially rearrange as they would lose support, but could keep undergoing further

31   dissolution until $n \to 1$), and upper-bounded by the point where the growing grains (spheres) outpace the

32   growing bonds (cylinders), i.e. the point at which growing cylinders are embedded into the growing

1 spheres, due to faster overall rate of growth of the spherical shape compared to the cylindrical one. This

2 happens when $R_g = \sqrt{H_c^2/4 + R_b^2}$. Further deposition beyond this point implies a second configuration,

3 at lower porosity, where only grains grow, hence the skeleton geometry is represented by large,

4 interpenetrating spheres. This second case is limited by the possible partial overlapping of spheres located

5 at opposite positions along the REV diagonal. Beyond this point, further deposition would imply a possible

6 residual very small porosity and a different geometry, which is not investigated here. Hence, the second

7 case applies to the range $\sqrt{H_c^2/4 + R_b^2} \leq R_g < H_c \sqrt{2}/2$.

8   Starting from an initial sample configuration where $R_b = 0.02$ mm, $R_g = 0.05$ mm and $H_c = 0.11$ mm,

9 in Figure 4a the specific cross section area of cementing bonds a_b is plotted versus porosity, distinguishing

10 by different line types the two sub-cases discussed above (in the second configuration, the cross section

11 area at the intersection of overlapping spheres is used to compute a_b). The slope discontinuity in the

12 curves represents the passage between the first and second geometrical configuration. Expectedly, it can

13 be observed that $a_b \to 1$ when $n \to 0$ and $a_b \to 0$ when $n \to 1$. Sensitivity to the relative proportions of

14 grains and bonds is also explored in Figure 4a by plotting two extra curves characterized by different

15 combinations of R_b, R_g and H_c. In Figure 4b the equivalent curves obtained with the modelling

16 approach described in Section 4 are shown, starting from the same geometrical configuration, where

17 $N_b = 6N_g$, for different values of exponent θ (cf. eqn. (22)) and for $\delta = 0.3$.

18   In Figure 5a the specific reactive surface area a_r obtained by microscopic calculation is plotted versus

19 porosity, for two different combinations of initial R_b, R_g and H_c values. It can be noticed that, as

20 expected, the specific reactive surface tends to zero at both limits of null and unit porosity.

21 Correspondingly, in Figure 5b the macroscopic calculation results obtained using model eqn. (18) are

22 drawn for two different values of parameter β.

23   Comparison between the two sets of curves described above suggests that calculations of a_b and a_r

24 respectively obtained with eqn. (22) and eqn. (18) provide a satisfactory representation of the material's

25 microstructure.

26   **5.   Selection of constitutive parameters and initial values**

27   Compared to the standard critical state framework, additional parameters have been introduced in the

28 micro-mechanically based constitutive model described above. Overall, the parameters featuring in this

29 model can be grouped into four families, namely: four constitutive parameters describing the material's

30 uncemented behavior (λ, ϕ_{cv}, E_g, ν_g), three constitutive parameters describing the mechanical properties

1   of the cementing material (σ_{rc} and σ_{rt}) and of completely cemented soil (E_b), two constitutive

2   parameters describing the mechanically-induced destructuration (A, k_1) and one parameter to describe

3   chemical healing (k_2), and finally five parameters for describing the macroscopic evolution of specific

4   reactive surface area and the specific cross section area of cementing bonds (β, γ, δ, θ, a_{r0}). The latter five

5   parameters, resulting from the above presented, bespoke micro-to-macro formulation, constitute the most

6   innovative aspect of the proposed model, compared to previously published works.

7   Furthermore, the model needs the definition of the initial values of a number of quantities. In particular,

8   in addition to the usual definition of the initial porosity n_0 and of the uncemented preconsolidation

9   pressure p_c, six new quantities are needed to describe the initial microscopic geometry, namely: the

10   number of grains, of cementing bonds and of active bonds (N_g, N_b, N_{ba}) and the geometric characteristics

11   of the grains (R_g) and of the bonds (R_b, d).

12   In light of the above described features, it is useful to discuss how the constitutive parameters on the

13   one hand, and the initial values of the quantities describing the initial conditions on the other hand, can be

14   selected.

15   The number of grains N_g can be selected from the solid mass of the grains (coinciding with the total

16   solid mass minus the solid mass of the cementing bonds), the specific gravity of the grains and the mean

17   grain radius R_g. The number of cementing bonds N_b can be evaluated from N_g and an estimate of the

18   coordination number, which is assumed to correspond to the number of bonds per grain. The number of

19   active bonds N_{ba} ranges between 0 and N_b, and can be reasonably estimated to be equal to N_b for an

20   undamaged cemented material. All quantities mentioned above, together with the geometric

21   characteristics of the grains and of the bonds, can be estimated from examining thin sections of the

22   microstructure of the cemented material. Useful hints for the selection of the coordination number can be

23   obtained from theoretical and experimental evaluations of the coordination number of random arrays of

24   spheres in contact with each other (e.g. [50]). Such studies provide estimations of the coordination number

25   of the order of 4-8 at large porosities and 8-12 at low porosities. In any case, precious information can be

26   also obtained from quantitative chemical analyses, providing for instance the variation of solid mass of the

27   sample (coinciding with the mass of dissolved bonds - and solid grains, if these are chemically active) at

28   different degrees of chemical interaction, possibly related to representative thin sections of the evolving

29   microstructure.

30   The elastic stiffness of the completely cemented soil E_b can be reasonably approximated with that of

31   the cementing material. Thus, the three constitutive parameters needed to describe the mechanical

properties of cementing material (E_b, σ_{rc} and σ_{rt}) can be selected from the literature, making reference to the intact material constituting the cementing bonds. It is worth adding that from standard tests (unconfined compression tests, isotropic compression tests and Brazilian tests), using trial-and-error procedures, it is possible to estimate the two positive quantities p_{tens} and p_{comp} representing the increase of tensile and compressive strength, due to the presence of cementation bonds, and the value of the uncemented preconsolidation pressure p_c (which should however be evaluated, if possible, also taking into account the behavior of the uncemented material). As a result, in order to avoid an over-constraint in the selection of p_{tens} and p_{comp} (due to the fact that p_{tens} and p_{comp} are evaluated from both micro-geometry quantities and macro mechanical experiments), the coordination number and the mechanical properties of the cementing material (σ_{rc} and σ_{rt}) need to be adjusted to achieve consistency between the two evaluations of p_{tens} and p_{comp}. Anyway, the evolution of p_{tens} and p_{comp} (from unconfined compression tests, isotropic compression tests and Brazilian tests) associated with the corresponding variation of the solid mass of the sample, at different degrees of chemical interaction, is certainly a valuable information for the precise calibration of the whole model.

The constitutive parameters describing the uncemented behavior (λ, ϕ_{cv}, E_g, ν_g) and the related initial value of the uncemented preconsolidation pressure p_c, should in principle be evaluated on the uncemented material (e.g. [51]). However, this is not always an easy task, thus these parameters are often evaluated by a trial-and-error procedure performed on the cemented material only. This obviously involves a higher level of uncertainty in the evaluation of p_{tens}, p_{comp} and of p_c.

Finally, the constitutive parameters describing mechanically-induced destructuration A and k_1 can be evaluated from the post-peak response in triaxial compression and post-yield behavior in isotropic compression tests. In this case, however, great care must be taken to account for the possible occurrence of shear or compaction bands, that can deeply affect the conventional response of the sample [52], [53], implying the impossibility to calibrate the model assuming a homogeneously deforming sample. Parameter k_2 describing chemical healing can be in principle calibrated on mechanical (e.g. uniaxial compression) tests carried out on samples of bonded geomaterial subjected to increasing degrees of cementation, although this parameter is not used in the model validation presented in Section 6 (see Table 1), since reference is made to chemo-mechanical weakening experiments only.

6. Model validation

The above described model was numerically integrated through a fully implicit, backward Euler integration scheme, showing adequate convergence. From the macroscopic, constitutive point of view, as

specified in Section 3.1, an extended version of Cam Clay yield function and hardening relationship were implemented. An associated flow rule was adopted for the sake of simplicity.

The model capabilities to reproduce the experimental chemo-mechanical behavior of bonded geomaterials were tested by simulating a series of loading paths along the lines of experimental datapoints reported in the literature, after having deduced the relevant parameters as much as possible from published data.

6.1 Simulation of chemo-mechanical loading paths

To support validation of the model in simulating chemo-mechanical loading paths in materials with both reactive grains and bonds, reference can be made to the extensive set of experiments reported by Ciantia et al. [31], Ciantia and Hueckel [5] and Castellanza and Nova [30] on a number of samples of calcarenite subject to different combinations of acidic weathering and mechanical loading.

As a first example, the model is tested by simulating unconfined compression tests on saturated calcarenite, by first reproducing an acid weathering phase and subsequently a mechanical loading phase, and comparing the simulations with the experimental data of [31]. In this context, a variable expressing the 'degree of dissolution' can be introduced as $\xi = M_{dis}/M_0$, where M_{dis} represents the dissolved mass and M_0 the initial mass of reacting solids, so that ξ =0 for the unweathered material and ξ =1 at complete dissolution of the reacting solids.

The parameter values adopted for this set of simulations on calcarenite are shown in Table 1 (set #1). In particular, the initial average grain radius and bond radius and length were selected upon evaluating thin section photographs reported in [31]. The initial porosity was chosen from a reference range of 0.4-0.6, established from Table 1 of [31].

As discussed in section 3.2, the equivalent elastic modulus of the bonded material E depends on both the elastic properties of calcite cement and of the unbonded granular material, and is calculated upon taking the second derivative of the free elastic energy density (5) with respect to elastic strain. Thus, we obtain an expression of the form

$$E = E_g \left(1 - a_b{}^\alpha\right) + E_b a_b{}^\alpha \qquad (24)$$

where E_g and E_b the elastic moduli of uncemented solid skeleton and of completely cemented soil (which is approximated with that of pure calcite) respectively, and parameter α =1.8. It should be noted that eqn. (24) is also consistent with mixture theory-based rules to obtain the equivalent parameters of a composite mass, typically employed in soil improvement calculations (e.g. see [54]). As initial value, estimating

1 $E_b \approx 150$ GPa from sonic wave velocity data on calcite after [55] and $E_g \approx 5$ Mpa, using (24) we obtain an

2 equivalent initial elastic modulus $E_0 \simeq 117$ Mpa.

3   To obtain the initial values of p_{tens} and p_{comp} via eqns. (2), and thus define the initial yield locus size, the

4 values of compressive and tensile strength of calcite can be deduced from the literature. Goodman [55]

5 reports q_c =90 Mpa and $q_t = q_c/30$ respectively, for carbonate rocks. However, for a more realistic

6 reproduction of experimental trends, also considering the data set on the compressive and tensile strength

7 of a number of saturated calcarenite samples reported by Ciantia et al. ([31], Table 1), we choose here

8 σ_{rc} =90 Mpa and σ_{rt} =8 Mpa.

9   ### 6.1.1   Chemo-mechanical uniaxial compression tests

10   In Figure 6, simulations of stress-strain curves during unconfined compression tests are plotted at

11 different values of ξ, together with analogous experimental data. To adequately reproduce experimental

12 conditions, the simulation consisted of two steps, namely of a first step reproducing exposure to an acid

13 solution up to the target value of ξ, and of a second step simulating the unconfined compression test in

14 the weathered material. The reproduction of experimental data is especially accurate until the ultimate

15 strength is attained. After the peak, simulations exhibit a smaller amount of softening than experiments,

16 overall showing a less markedly fragile behavior. Since the post-peak response is typically deeply affected

17 by shear or compaction banding which leads the conventional behavior to be much different from that of a

18 homogeneously deforming sample (cf. [52], [53]), additional ad-hoc constitutive assumptions were not

19 introduced for more accurate reproduction of this phenomenon.

20   More details of the acid weathering phase, that precedes mechanical loading, are simulated in Figure 7,

21 where the ratio of the current specific cross section area of bonds over its initial value before weathering,

22 a_b/a_{b0}, is plotted versus ξ. Since from eqn. (2) both material's compressive and tensile strength evolve

23 with the specific cross-section area of bonds, the same curve also represents the simulated evolution with

24 chemical dissolution/deposition of ratios p_{tens}/p_{tens0} and p_{comp}/p_{comp0}. In the same plot, both

25 experimental data of normalized tensile strength measured with Brazilian tests [31], and the data points of

26 a_b/a_{b0} obtained by Ciantia et al. [31] by means of image processing of thin sections of calcarenite, are

27 reported, for comparison with the simulated data. The tensile strength data exhibit a very similar trend to

28 simulations. In contrast, despite the experimentally observed trends of variation with ξ of both tensile and

29 compressive strength being curved, the normalized cross sectional bond area derived from image

30 processing seems to decrease linearly with ξ, hence the simulations cannot reproduce them accurately.

31 However, both the numerical and the experimental data, respectively with a curved and a linear trend, lead

1 to identify the 'critical' value of ξ corresponding to the vanishing of bond cross-sectional areas to about

2 0.4-0.5.

3   In Figure 8 and Figure 9 the simulated normalized uniaxial compressive strength UCS/UCS$_0$ (i.e. ratio of

4 weathered to initial UCS, obtained by extracting peak stress values from several uniaxial compression

5 simulations in the range ξ =0-0.35) and the normalized elastic modulus E/E_0 respectively are plotted

6 versus ξ, and compared to the corresponding experimental data, showing satisfactory agreement in both

7 cases.

8   Further, the parameter set #1 of Table 1 was also used to simulate oedometer tests on calcarenite

9 samples previously subjected to different degrees of weathering. In Figure 10, satisfactory simulations are

10 shown in terms of vertical strain versus vertical stress, at different degrees of dissolution. Experimental

11 data from [31] are also reported in the graph for comparison.

12   **6.1.2   Chemo-mechanical oedometer tests**

13   A second, different set of chemo-mechanical simulations was performed to reproduce the special

14 oedometer tests, allowing measurement of radial stress, carried out on calcarenite by Castellanza and Nova

15 [30], in which the material was subject to acid weathering after the application of a constant vertical load.

16 For consistency, presuming that the tested calcarenite belongs to the same formation as that tested by

17 Ciantia et al. [31], the same parameter set #1 of Table 1 was adopted, despite the different experimental

18 conditions.

19   In Figure 11 the stress path of Castellanza and Nova [30]'s oedometer test in the $\left(p, \, q \right)$ plane is

20 simulated, and fittingly compared to experimental data. The path A-B represents the mechanical loading

21 phase. Upon reaching point B, the vertical load is kept constant and the acid weathering phase starts,

22 gradually causing an increase of radial stress, revealing as a linear decrease of deviatoric stress with

23 increasing mean stress (path B-C).

24   In Figure 12a the simulated evolution of radial stress during the weathering phase of the test is shown as

25 a function of ξ. Similar experimental data are plotted in the same figure for comparison, however it should

26 be noted that the two plots are not exactly equivalent, since the experimental data are reported as a

27 function of time since the start of weathering (Fig. 11 of Castellanza and Nova [30]), and no information is

28 available to deduce the degree of dissolution ξ. The initial horizontal part of the simulation represents the

29 chemo-elastic phase at constant applied stress, at the end of which the shrinking yield locus attains the

30 stress point, and chemo-plastic loading starts. Along the same lines, in Figure 12b the simulated axial strain

31 during the weathering phase of the test is shown as a function of ξ, together with the experimental

32 measurements of axial strain as a function of time, for approximate comparison. To better explain these

simulation trends, in Figure 13a the simulated evolution of preconsolidation pressure p_c versus degree of dissolution is shown. It can be noted that only elastic loading occurs up to point D in the graph (also marked in Figure 12a), followed by plastic loading: an initial softening phase implies dilative volumetric behavior, until point E is reached (also marked in Figure 12b), representing a transition between dilative and contractive volumetric behavior. This point implies for the stress path the passage by the yield locus' horizontal tangent point, where the plastic volumetric strain rate is zero while the size of the yield locus continues to evolve (cf. Section 3.1). The evolution of ratio a_b/a_{b0} during the weathering phase is shown in Figure 13b against mean effective stress. It can be noticed that initially, in elastic conditions, the mean stress does not change with dissolution, and starts increasing only upon reaching plastic loading conditions.

6.2 Purely mechanical axisymmetric tests on bonded materials

The model was further tested by reproducing mechanical tests on bonded materials, without invoking chemical couplings. In this case, reference is made to the experimental evidence gathered by Lagioia and Nova [36], who presented a number of axisymmetric tests on a calcarenite. The set of model parameters adopted for these simulations is shown as set #2 in Table 1. Figure 14 shows experimental data and the relevant simulation of an isotropic compression test in terms of void ratio variation as a function of mean effective stress. The typical abrupt volumetric collapse at nearly constant stress, indicating destructuration of the material, is effectively reproduced by the model. In Figure 15 the comparison between the simulations and experimental results of a drained triaxial compression test at a constant cell pressure of 900 kPa is shown both in terms of deviatoric stress and of volumetric strain versus axial strain. While the stress-strain trend is correctly captured by the model, the numerical reproduction of experimental results in terms of volumetric versus axial strain is not as accurate, but still of comparable order of magnitude. The main source of inconsistency is related to the impossibility of simulating exactly the yield stresses in isotropic compression and triaxial compression. This inconsistency is related to the assumed shape of the yield surface, thus the simulations could be improved by substituting the yield surface of Cam Clay model with a yield surface having a less rounded shape in the axes origin (e.g., [56], [57]).

7. Conclusion

In this work an innovative, general two-scale modelling framework able to account for the key aspects of the coupled chemo-mechanical behavior of bonded granular materials is presented, and validated against experimental evidence. The proposed framework includes an integrated model for mass change of minerals, in the frame of an idealized evolving micro-scale structure of grains and bonds, subject to removal or addition of mineral mass, localized mechanical failure and chemical healing, and a macro-scale chemo-elasto-plastic model, where both the yield stress under isotropic compression and the isotropic tensile

strength depend on the material microstructural features, incorporating elasto-plastic coupling to describe the degradation of elastic properties due to mechanically induced debonding.

The key feature of the proposed model is the introduction of two variables: the specific reactive surface area and the mean cross sectional area of the bonds. The specific reactive surface area has the key role of governing the rate of chemical dissolution/precipitation (cementation) and depends on the current amount of cement (micro-fracturing induced by plastic strains is neglected in a first approximation). The mean cross sectional area of the bonds defines the increase/decrease of strength and stiffness due to cementation bonds and depends on bond breakage and on the amount of dissolution/cementation. The specific reactive surface area and the mean cross section area of the bonds are deduced from a micromechanical model, with the advantage of avoiding unphysical situations in which deposition could occur with no porous space available or dissolution could occur with no cementing material left.

In addition, the proposed framework permits to keep track of the evolution of important micromechanical quantities such as the number of active (i.e. non-broken) bonds and their cross sectional area. For the sake of simplicity, the distribution of bonds and their cross sections are assumed isotropic and the model presentation is based on simple linear isotropic elasticity and Cam Clay yield function. The proposed constitutive framework is not however limited to these simple assumptions and could be straightforwardly applied to more complex elasticity models and yield functions. Moreover, the proposed framework could be easily extended to situations involving the presence of different families of cementation bonds characterized by different strengths and chemical dissolution properties, such as those experimentally observed by Ciantia and Hueckel [5] and Ciantia et al [31] on calcarenite.

It can be concluded that the presented model provides a powerful and flexible framework for adequately reproducing different experimental chemo-mechanical loading paths. Due to limited availability of experimental results in the literature, only a few examples focused on the behavior of calcarenite are presented here. However, it is worth remarking that the model is to be intended as an open framework rather than being specialized on a particular material type. Different additional effects, such as mechanical anisotropy, could easily be incorporated depending on modeling needs.

References

[1]   Terzaghi K. Mechanism of landslides. Cambridge: Harvard University, Department of Engineering; 1950.

[2]   Moore R. The Chemical and Mineralogical Controls Upon The Residual Strength Of Pure And Natural Clays. Geotechnique 1996; 41(1): 35-47.

[3]   Moore R, Brunsden D. Physico-chemical effects on the behaviour of a coastal mudslide. Geotechnique 1996; 46(2): 259-278.

[4]   Chigira M, Oyama T. Mechanism and effect of chemical weathering of sedimentary rocks. Engineering Geology 2000; 55: 3-14.

[5]   Ciantia MO, Hueckel T. Weathering of submerged stressed calcarenites: chemo-mechanical coupling mechanisms. Geotechnique 2013; 63 (9): 768-785.

[6]   Hueckel T, Hu LB. Feedback mechanisms in chemo-mechanical multi-scale modeling of soil and sediment compaction. Computers and Geotechnics 2009; 36, 934-943.

[7]   Castellanza R, Nova R, Gerolymatou E. An attempt to predict the failure time of abandoned mine pillars. Rock Mechanics And Rock Engineering 2008; 41(3): 377-401.

[8]   Zhao Y, Cui P, Hu LB, Hueckel T. Multi-scale chemo-mechanical analysis of the slip surface of landslides in the Three Gorges, China. Science China Technological Sciences 2011; 54: 1757-1765.

[9]   Andre L, Azaroual M, Menjoz A. Numerical Simulations of the Thermal Impact of Supercritical CO2 Injection on Chemical Reactivity in a Carbonate Saline Reservoir. Transport in porous media 2010; 82 (1):247-274.

[10]   Nguyen MT, Bemer E and Dormieux L. Micromechanical modeling of carbonate geomechanical properties evolution during acid gas injection. In: 45th US Rock Mechanics/Geomechanics Symposium. San Francisco, CA; June 26th – 29th, 2011.

[11]   Hu LB, Hueckel T. Coupled chemo-mechanics in evolving permeability in geomaterials. In: Computational Geomechanics (ComGeo II). Cavtat-Dubrovnik; 2011; p. 599-608.

[12]   Kahlweit M. Ostwald Ripening of Precipitates. Advances in Colloid and Interface Science 1975; 5 (1): 135.

[13]   Sjoberg EL. A fundamental equation for calcite dissolution kinetics. Geochim. Cosmochim. Acta 1976; 40: 441–447.

[14]   Rimstidt JD, Barnes DL. The kinetics of silica-water reaction, Geochim. Cosmochim. Acta 1980; 44:1683-1699.

[15]   Hu LB, Hueckel T. Coupled chemo-mechanics of intergranular contacts: toward a three-scale model. Computers and Geotechnics 2007; 34(4), 306-327.

[16]   Hueckel T, Hu LB. Feedback mechanisms in chemo-mechanical multi-scale modeling of soil and sediment compaction. Computers and Geotechnics 2009; 36: 934-943.

[17]   Hueckel T. Reactive Plasticity for Clays during Dehydration and Rehydration. Part I: Concepts and Options. International Journal of Plasticity 2002; 18(3): 281-312.

[18]   Loret B, Hueckel T, Gajo A. Chemo-mechanical coupling in saturated porous media: elasto-plastic behaviour of homoionic expansive clays. International Journal of Solids and Structures 2002; 39: 2773-2806.

[19]   Gens A, Nova R. Conceptual bases for a constitutive model for bonded soils and weak rocks. In: proc. International Symposium on Geotechnical Engineering of Hard Soils - Soft Rocks, Athens, Greece; 1993.

[20]   Nova R. Modelling the weathering effects on the mechanical behaviour of granite. In: Constitutive modelling of granular materials 2000, D Kolymbas, editor. Springer, Berlin. p. 397–411.

[21]   Nova R, Castellanza R, Tamagnini C. A constitutive model for bonded geomaterials subject to mechanical and/or chemical degradation. Int J Num Anal Meth Geomech 2003; 27(9):705–732.

[22]   Matsukura Y, Hirose T. Five year measurements of rock tablet weathering on a forested hillslope in a humid temperate region. Engng Geol. 1999; 55: 69–76.

[23]   Kohler SJ, Dufaud F, Oelkers EH. An experimental study of illite dissolution kinetics as a function of pH from 1.4 to 12.4 and temperature from 5 to 50°C. Geochim Cosmochim Acta 2002; 67(19): 3583–3594.

[24]   Hueckel T. Coupling of elastic and plastic deformations of bulk solids 1976;

Meccanica 11(4): 227-235.

[25]   Maier G and Hueckel T. Nonassociated and coupled flow rules of elastoplasticity for rock-like material. Int. J. Rock. Mech. Min. & Sci. Geomech. Abstr. 1979; 16: 77-92.

[26]   Hueckel T. Discretized Kinematic Hardening in Cyclic Degradation of Rocks and Soils. Engineering Fracture Mechanics 1985; 21(4): 923-945.

[27]   Hueckel T, Tutumluer E. Modeling of elastic anisotropy due to one-dimensional plastic consolidation of clays. Computers and Geotechnics 1994; 16: 311-349.

[28]   Gajo A, Bigoni D. A model for stress and plastic strain induced nonlinear, hyperelastic anisotropy in soils. Int J Num Anal Meth Geomech 2008; 32 (7), p. 833-861.

[29]   Gajo A. Hyperelastic modelling of small-strain stiffness anisotropy of cyclically loaded sand. Int J Num Anal Meth Geomech 2010; 34(2), 111-134.

[30]   Castellanza R and Nova R. Oedometric tests on artificially weathered carbonatic soft rocks. J. of Geotechnical and Geoenvironmental Eng. ASCE 2004; 130(7): 28 – 739.

[31]   Ciantia MO, Castellanza R and di Prisco C. Experimental study on the water-induced weakening of calcarenites. Rock Mech. Rock Eng. 2014; DOI 10.1007/s00603-014-0603-z.

[32]   Eide KE. CO_2 Sequestration: The effect of carbonate dissolution on reservoir rock integrity. MSc thesis. NTNU Trondheim, Norway; 2012.

[33]   Hangx S, van der Linden A, Marcelis F, Bauer A. The effect of CO_2 on the mechanical properties of the Captain Sandstone: Geological storage of CO_2 at the Goldeneye field (UK). International Journal of Greenhouse Gas Control 2013; 19: 609–619.

[34]   Risnes R, Madland MV, Hole M and Kwabiah NK. Water weakening of chalk – Mechanical effects of glycol and water. J. Pet. Sci. Eng. 2005; 48: 21-36.

[35]   Heggheim T, Madland MV, Risnes R and Austad T. A chemical induced enhanced weakening of chalk by seawater, J. Pet. Sci. Eng., 2005; 46: 171-184.

[36]   Lagioia R, Nova R. An experimental and theoretical study of the behaviour of a calcarenite in triaxial compression. Geotechnique 1995; 45(4): 633–648.

[37]   Gajo A, Muir Wood D. A new approach to anisotropic, bounding surface plasticity: general formulation and simulations of natural and reconstituted clays. Int J Num Anal Meth Geomech 2001; 25: 207-241.

[38]   HS Yu, Khong CD, Wang J, Zhang G. Experimental evaluation and extension of a simple critical state model for sand. Granular Matter 2005; 7: 213–225.

[39]   Yan WM, Li XS. A model for natural soils with bonds. Geotechnique 2011; 61 (2): 95-106.

[40]   Hueckel T. Water - Mineral Interaction in Hygro-Mechanics of Clays Exposed to Environmental Loads: a Mixture Theory Approach. Canadian Geotechnical Journal 1992; 29: 1071-108.

[41]   Gajo A, Loret B, Hueckel T. Electro-chemo-mechanical couplings and the elastic-plastic behaviour of heteroionic expansive clays. In: Chemo-Mechanical coupling in clays, C. Di Maio, T. Hueckel, B. Loret, editors. Rotterdam: Balkema; 2002. pp. 261-276.

[42]   Muir Wood D. Soil Behaviour and Critical State Soil Mechanics. New York: Cambridge University Press; 1990.

[43]   Roscoe KH, Burland JB. On the generalised stress-strain behaviour of 'wet' clay. Engineering Plasticity 1968; 535-609.

[44]   Willam KJ, Warnke EP. Constitutive models for the triaxial behavior of concrete. Proceedings of the International Assoc. for Bridge and Structural Engineering 1975; 19: 1- 30.

[45]   Desai CS, Siriwardane HJ. Constitutive laws for engineering materials. Englewood Cliffs: Prentice-Hall; 1984.

[46]   Voigt W. Ueber die Beziehung zwischen den beiden Elasticitätsconstanten isotroper Körper. Annalen der Physik 1889; 274: 573–587.

[47]   Reuss A. Berechnung der Fließgrenze von Mischkristallen auf Grund der Plastizitätsbedingung für Einkristalle. ZAMM - Journal of Applied Mathematics and Mechanics / Zeitschrift für Angewandte Mathematik und Mechanik 1929; 9: 49–58.

[48]   Haase R. Thermodynamics of Irreversible Processes. New York: Dover Publications; 1990.

[49]   Brantley S, Kubicki J, Art W. Kinetics of Rock-Water Interaction. New York: Springer; 2007.

[50]   Murphy WF. Effect of microstructure and pore fluids on the acoustic properties of granular sedimentary materials. PhD thesis. Stanford University, USA, 1982.

[51]   Gajo A, Muir Wood D. A new approach to anisotropic, bounding surface plasticity: general formulation and simulations of natural and reconstituted clays. Int J Num Anal Meth Geomech 2001; 25: 207-241.

[52]   Gajo A, Bigoni D, Muir Wood D. Multiple shear band development and related instabilities in granular materials. Journal of The Mechanics And Physics Of Solids 2004; 52(12), 2683-2724.

[53]   Gajo A, Muir Wood D, Bigoni D. On certain critical material and testing characteristics affecting shear band development in sand. Geotechnique 2007; 57(5): 449-461.

[54]   Ou C, Wu T, Hsieh H. Analysis of deep excavation with column type of ground improvement in soft clay. Journal of Geotechnical Engineering 1996; 122(9): 709–716.

[55]   Goodman RE. Introduction to rock mechanics. Chichester: John Wiley & Sons; 1989.

[56]   Nova R and Hueckel T. A unified approach to the modelling of liquefaction and cyclic mobility of sands. Soils and Foundations 1981; 21(4): 13-28.

[57]   Bigoni D, Piccolroaz A. Yield criteria for quasibrittle and frictional materials. International Journal of Solids and Structures 2004; 41(11-12), 2855-2878.

1   **List of Figures**

grains

bonds

a)   b)

2
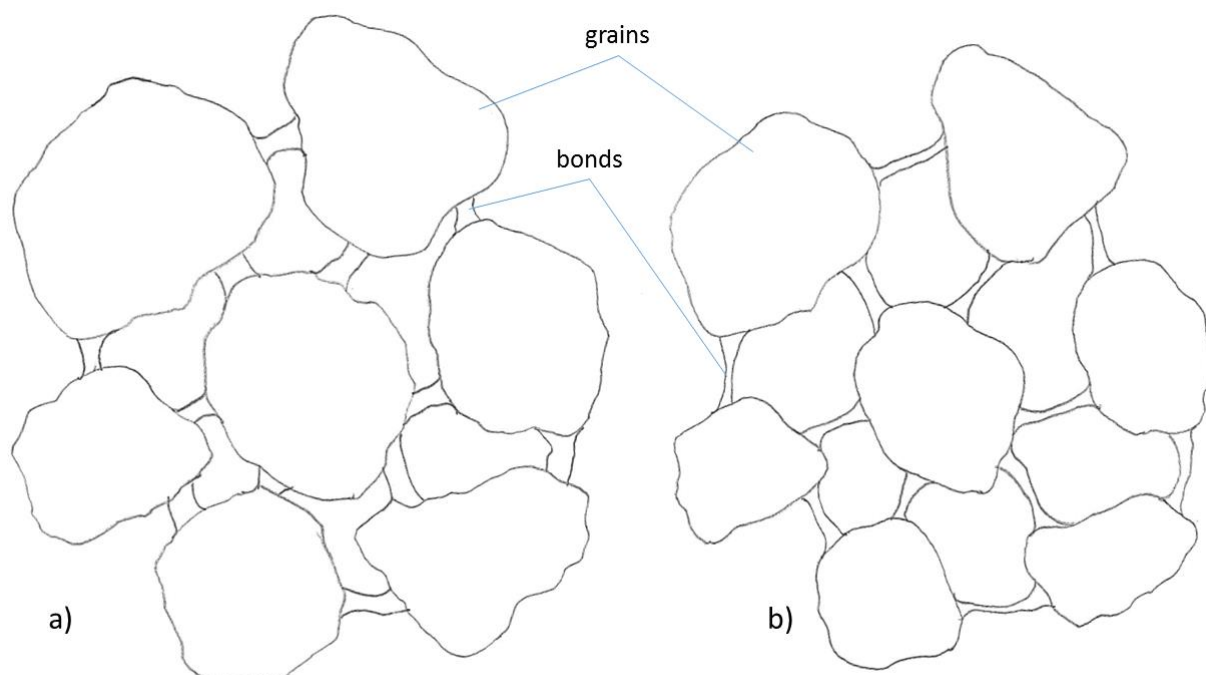
3   *Figure 1. 2D schematic inspired by microscope photographs of thin sections of calcarenite (e.g. [31])*
4   *showing a) an initial configuration and b) the material after some loss of mass due to chemical dissolution*
5   *of both grains and bonds, resulting in a porosity increase.*
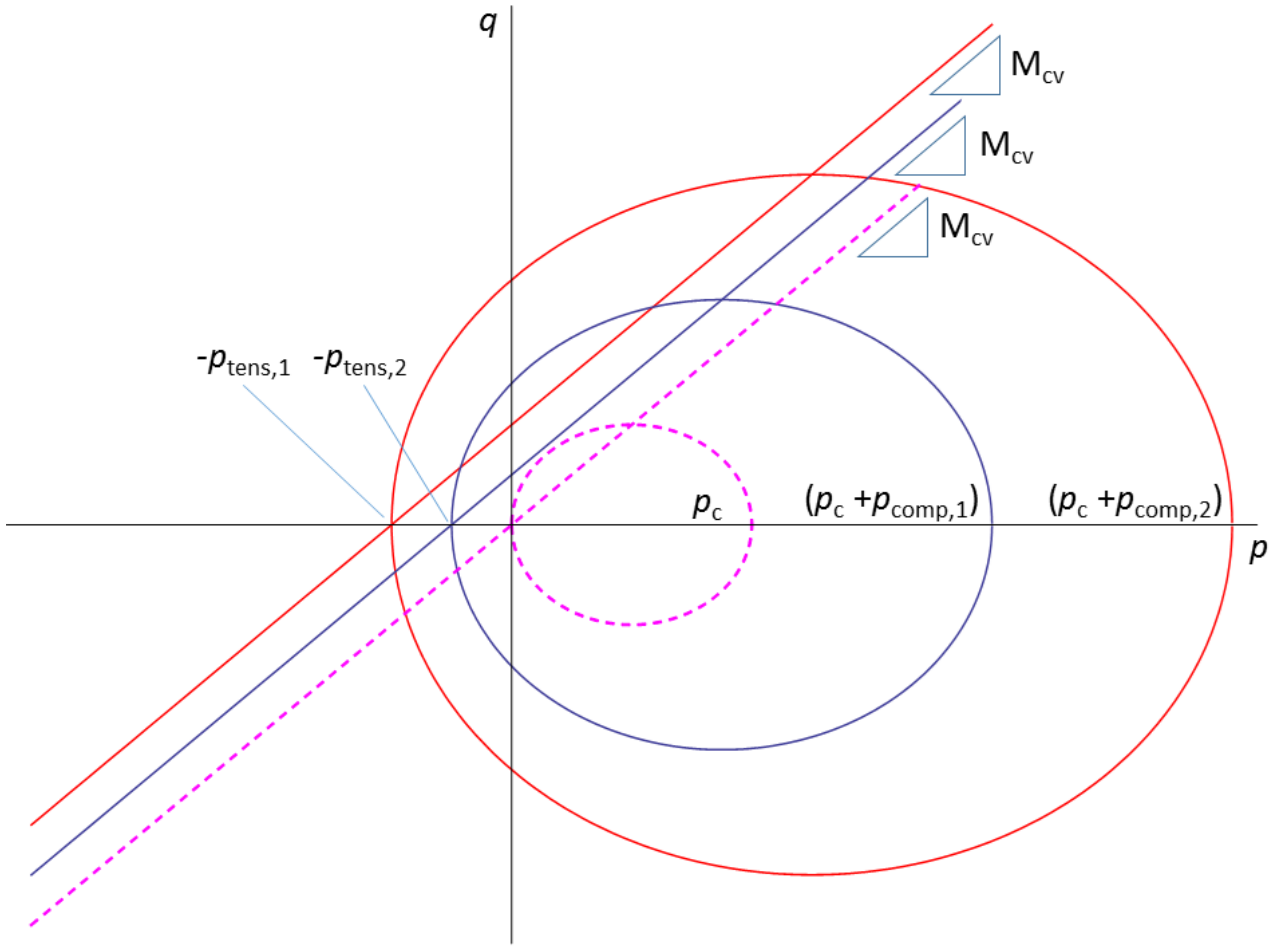
2   *Figure 2. Change of size of yield surface with changing cementation/destructuration (i.e. at different*

3   *values of p_{tens} and p_{comp}) in terms of invariants (p, q). The dashed surface represents the uncemented state,*

4   *in which $p_{tens}=p_{comp}=0$.*
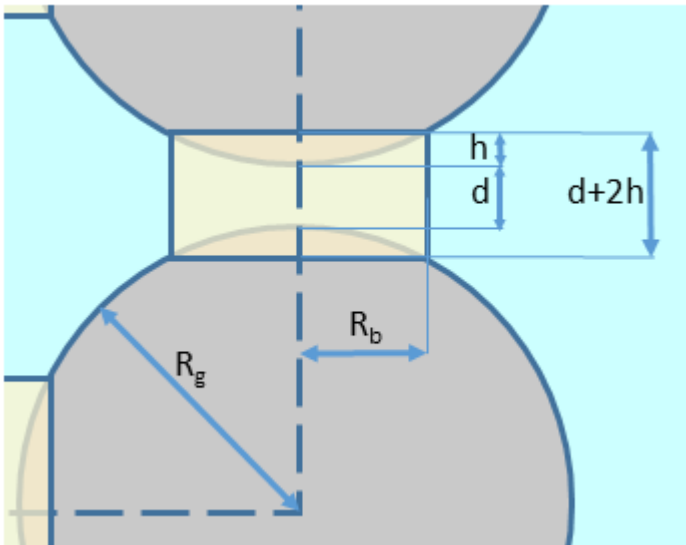
5

6   *Figure 3. Schematic of the considered simplified geometry at large porosity, in a general case where the*

7   *spherical grains are not in direct contact, but they are linked by cylindrical bonds.*
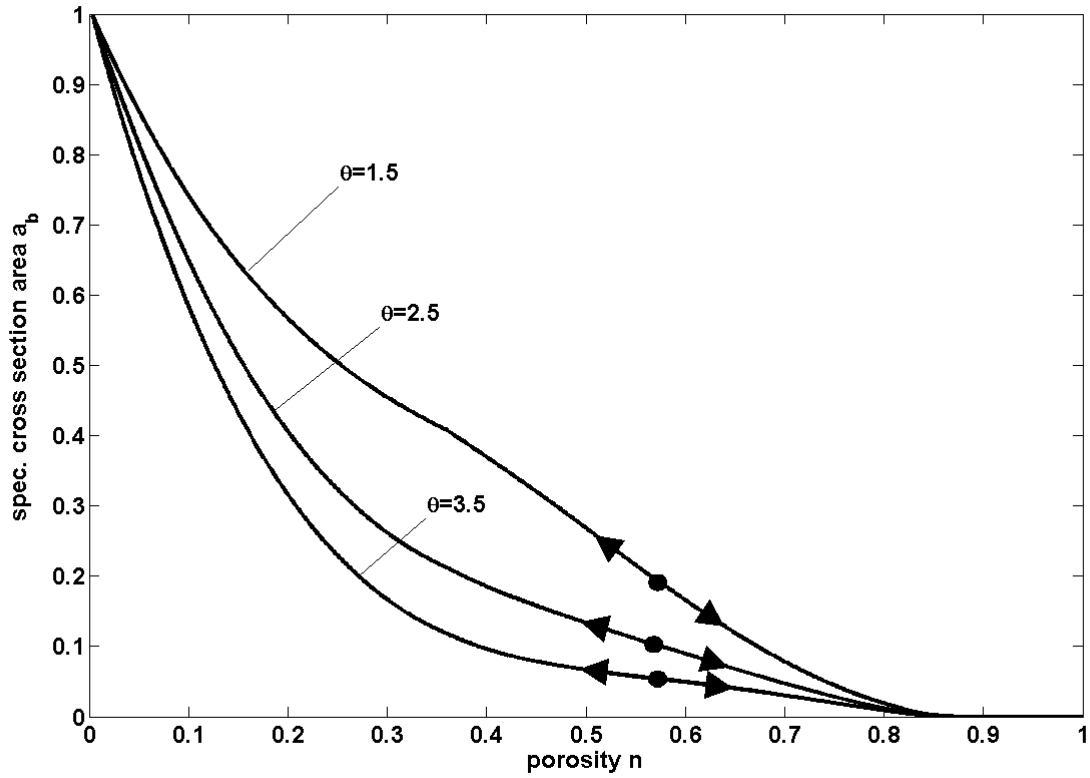
1
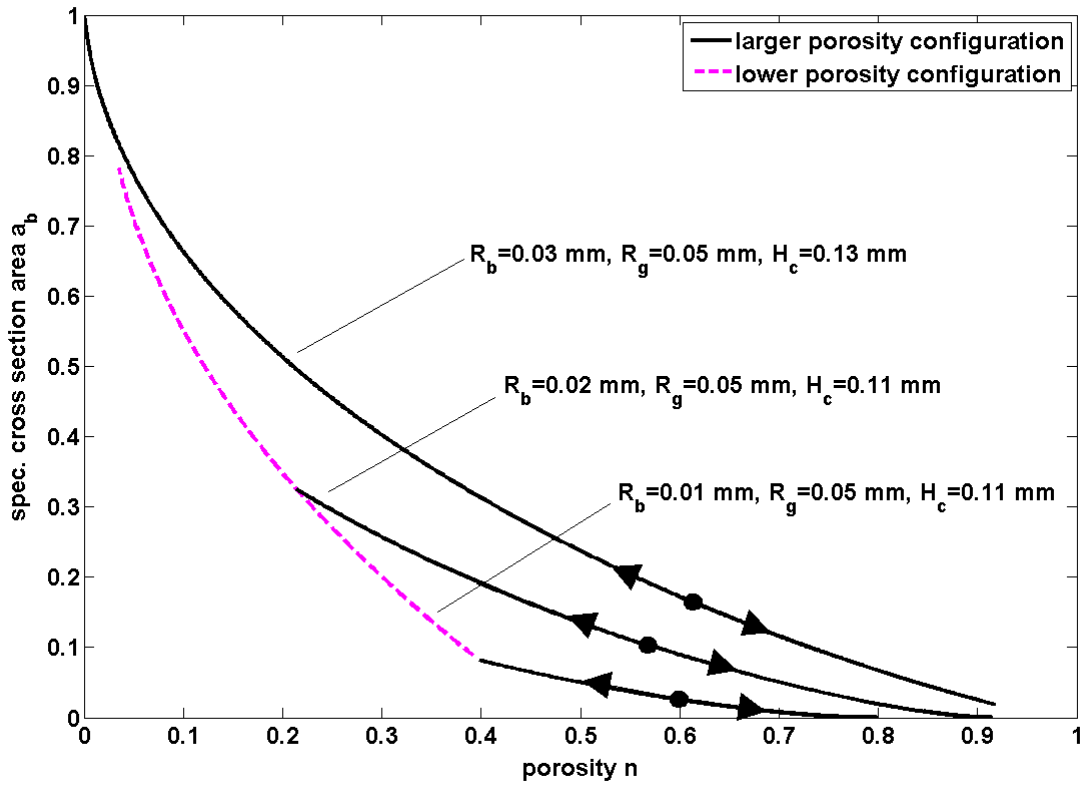
2

3   *Figure 4. Specific cross section area of cementing bonds versus porosity during dissolution/deposition*

4   *(the dots mark the initial porosity). a) microscale calculation according to three different intial geometrical*

1 *configurations, b) macroscopic calculation with model equation (22) for three different values of parameter*

2 θ *and for* δ*=0.3.*

3

1

2
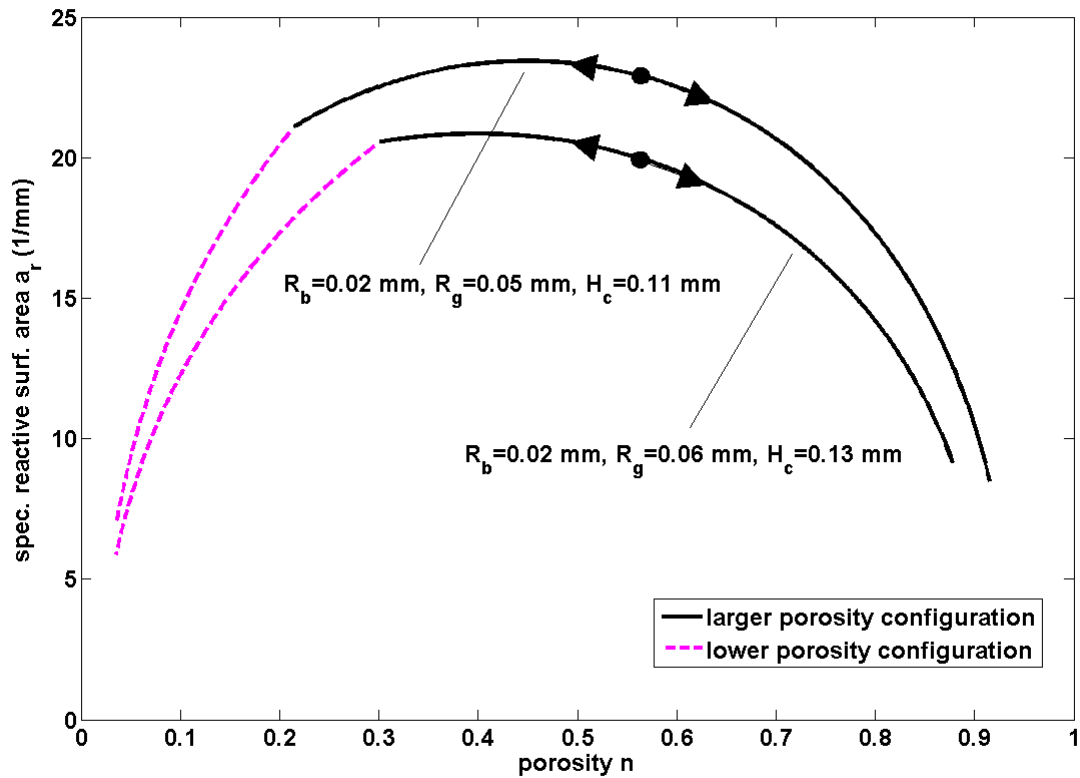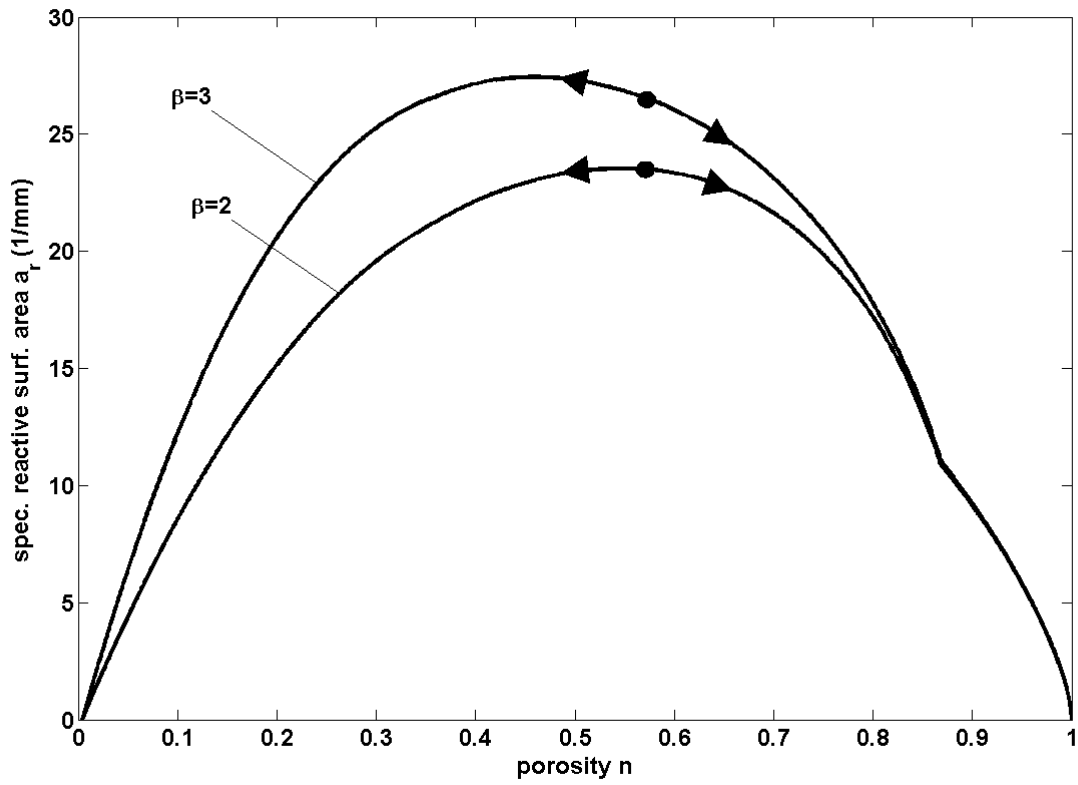
3   *Figure 5. Specific reactive surface area versus porosity during dissolution/deposition (the dots mark the*

4   *initial porosity). a) microscopic calculation according to two different intial geometrical configurations, b)*

5   *macroscopic calculation with model equation (18) for two different values of parameter β.*

1
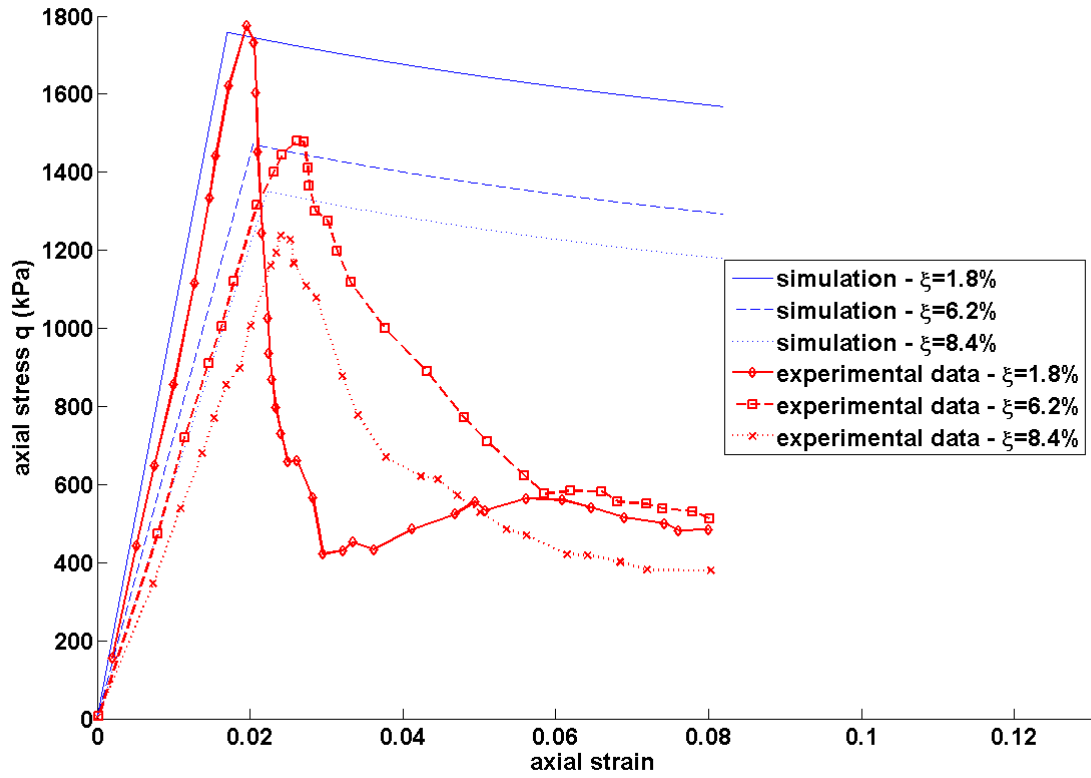
2
3   *Figure 6. Comparison of simulations and experimental data [31] in terms of deviatoric (axial) stress versus*

4   *axial strain in unconfined compression tests on calcarenite, carried out after weathering up to three*

5   *different values of degree of dissolution.*

6
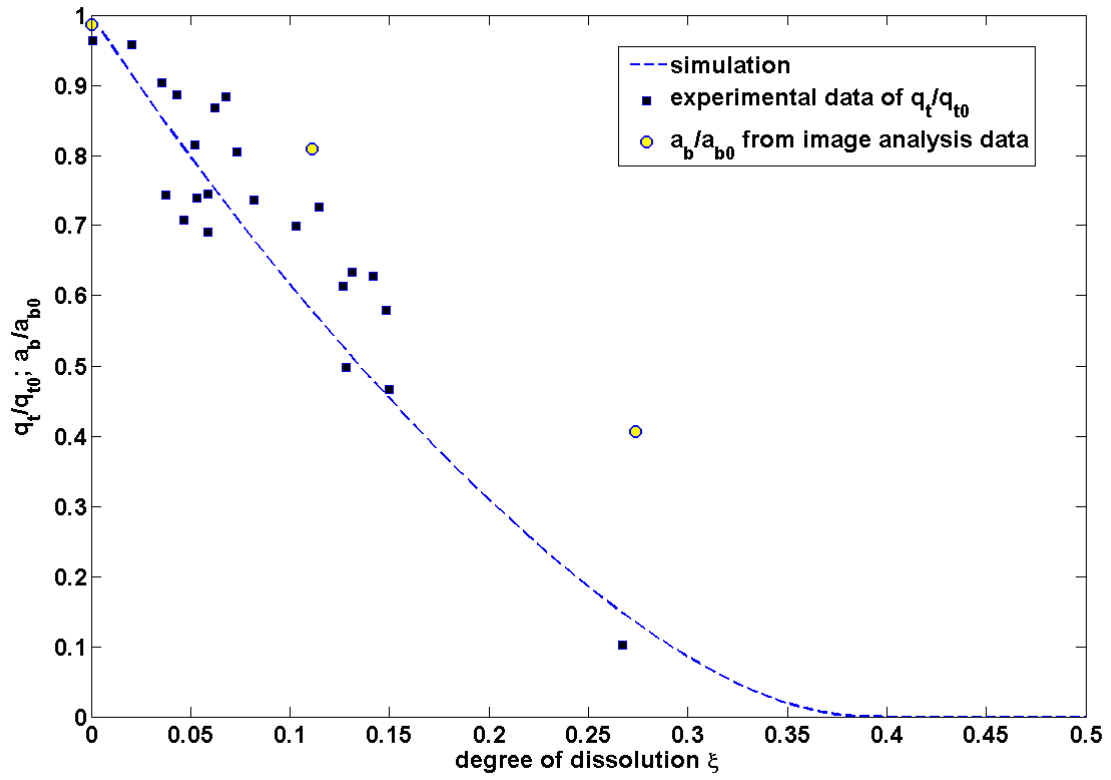
1
2 *Figure 7. Comparison of simulations and experimental data in terms of normalized area of bonds, or*

3 *equivalently normalized tensile strength, versus the degree of dissolution. The experimental data are taken*

4 *from Ciantia et al. [31]'s Brazilian test results.*

5
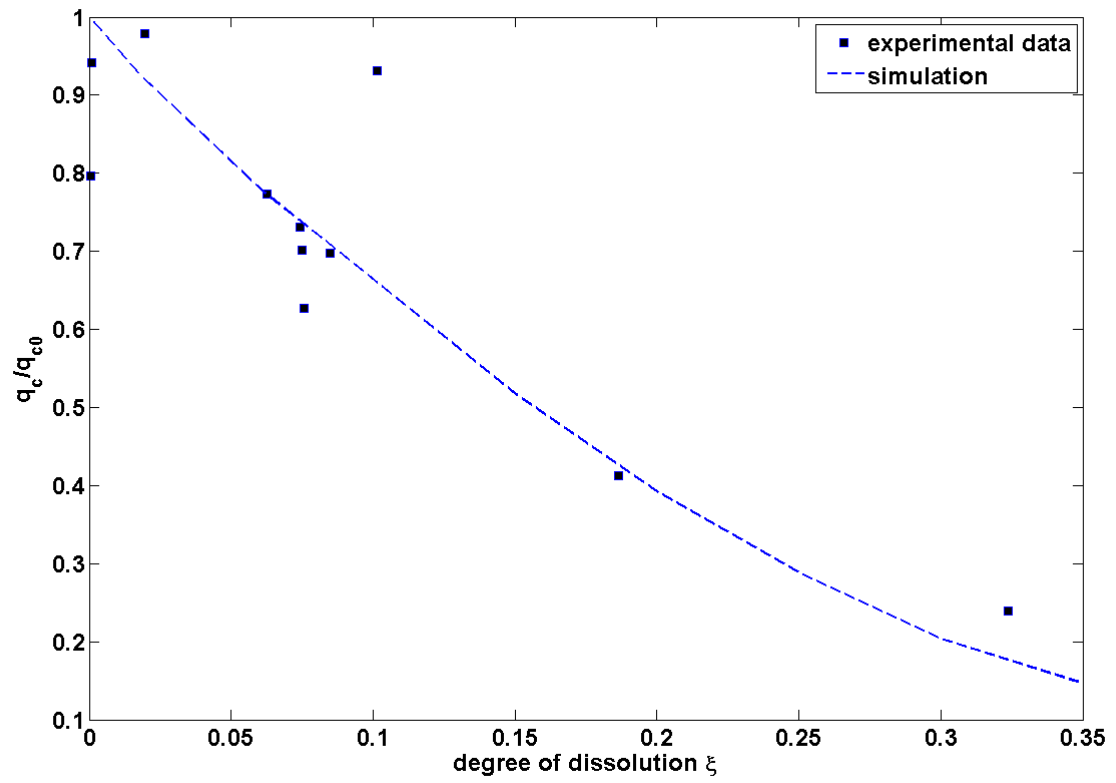
1
2 *Figure 8. Comparison of simulations and experimental data in terms of normalized UCS versus the degree of*

3 *dissolution. The experimental data are taken from Ciantia et al. [31]'s uniaxial compression test results.*

4
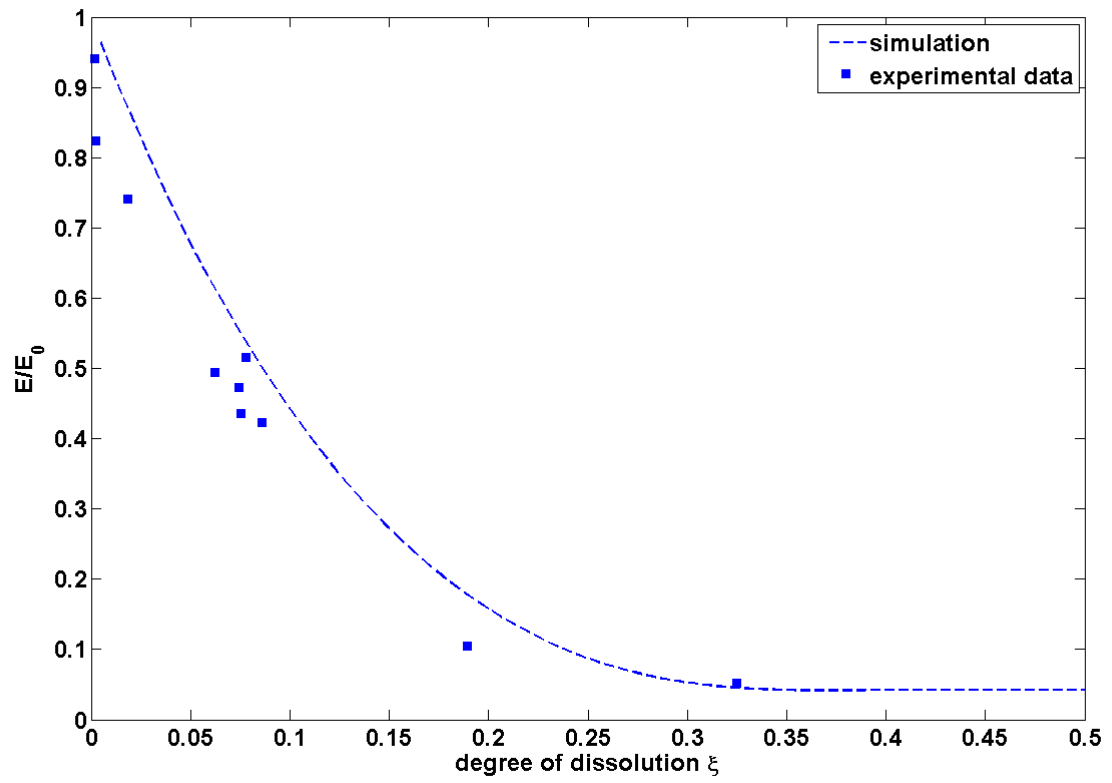
1
2 *Figure 9. Comparison of simulations and experimental data in terms of normalized elastic modulus versus*
3 *the degree of dissolution. The experimental data are taken from Ciantia et al. [31]'s uniaxial compression*
4 *test results.*

5
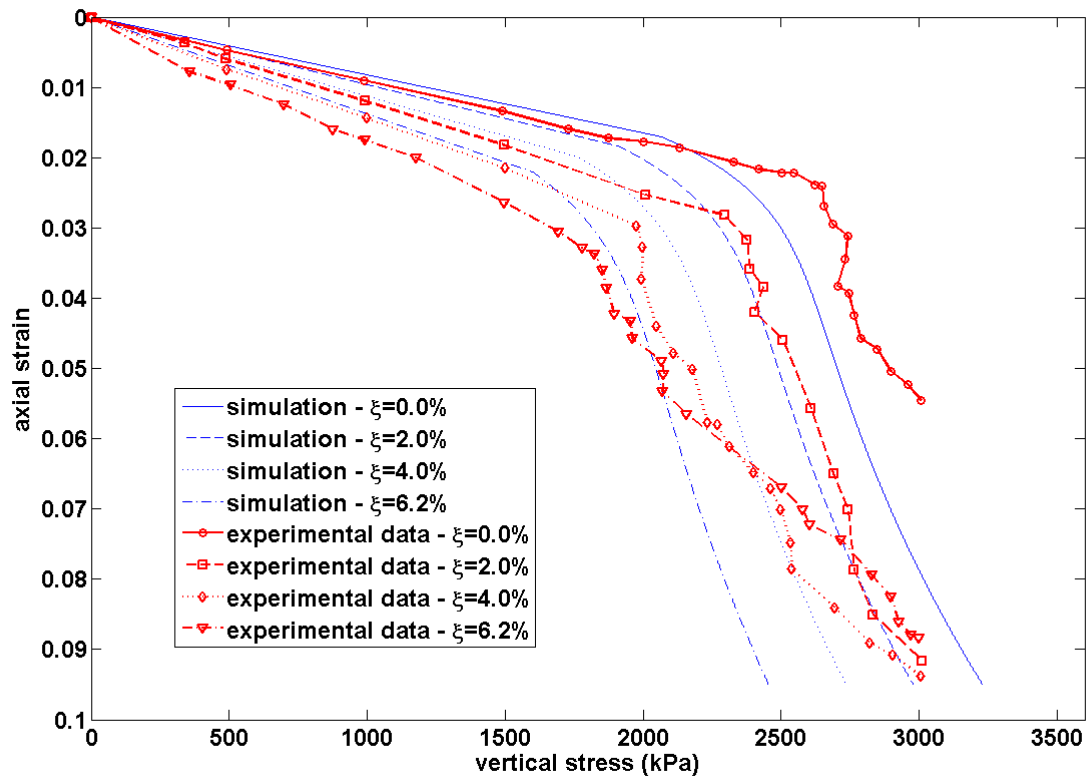
1
2   *Figure 10. Comparison of simulations and experimental data [31] in terms of axial strain versus vertical*
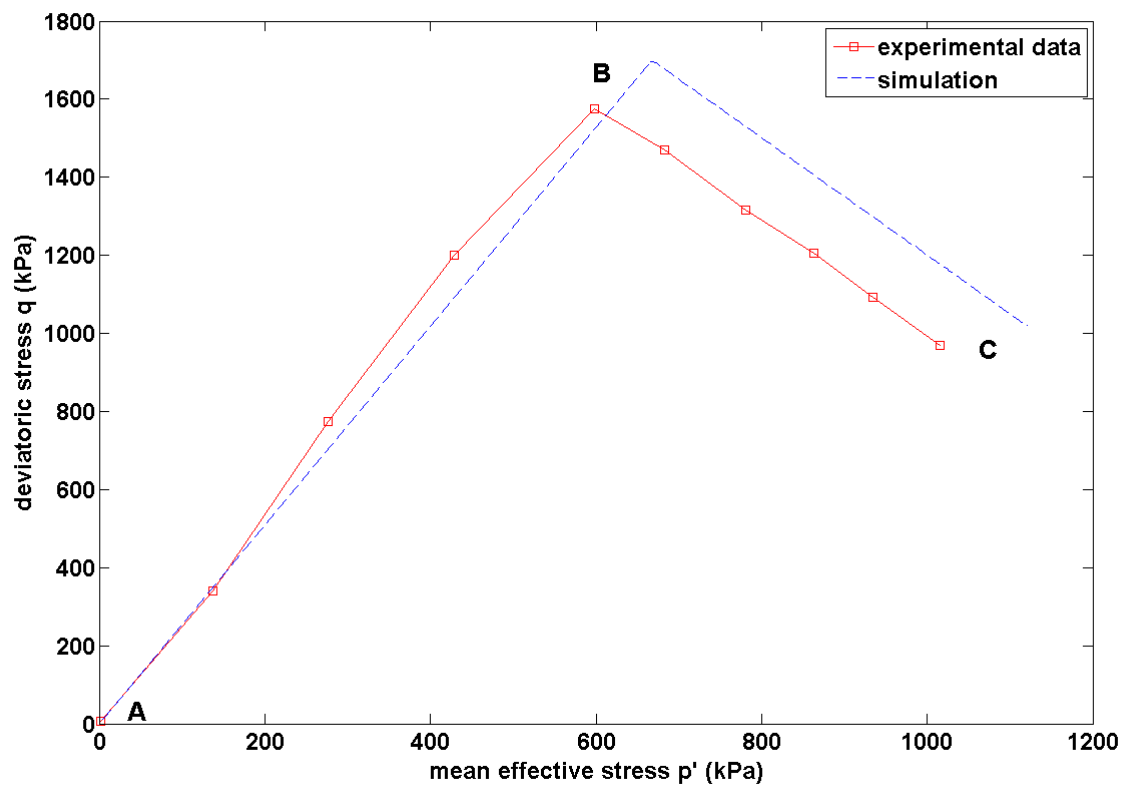3   *stress in oedometer tests on calcarenite, carried out after weathering up to four different values of degree*
4   *of dissolution.*

5

1
2 *Figure 11. Comparison of simulations and experimental data [30] in terms of deviatoric stress versus mean*

3 *effective stress in an oedometer test on calcarenite. Path A-B represents the loading phase in unweathered*

4 *conditions, path B-C represents the acid weathering phase at constant applied load.*
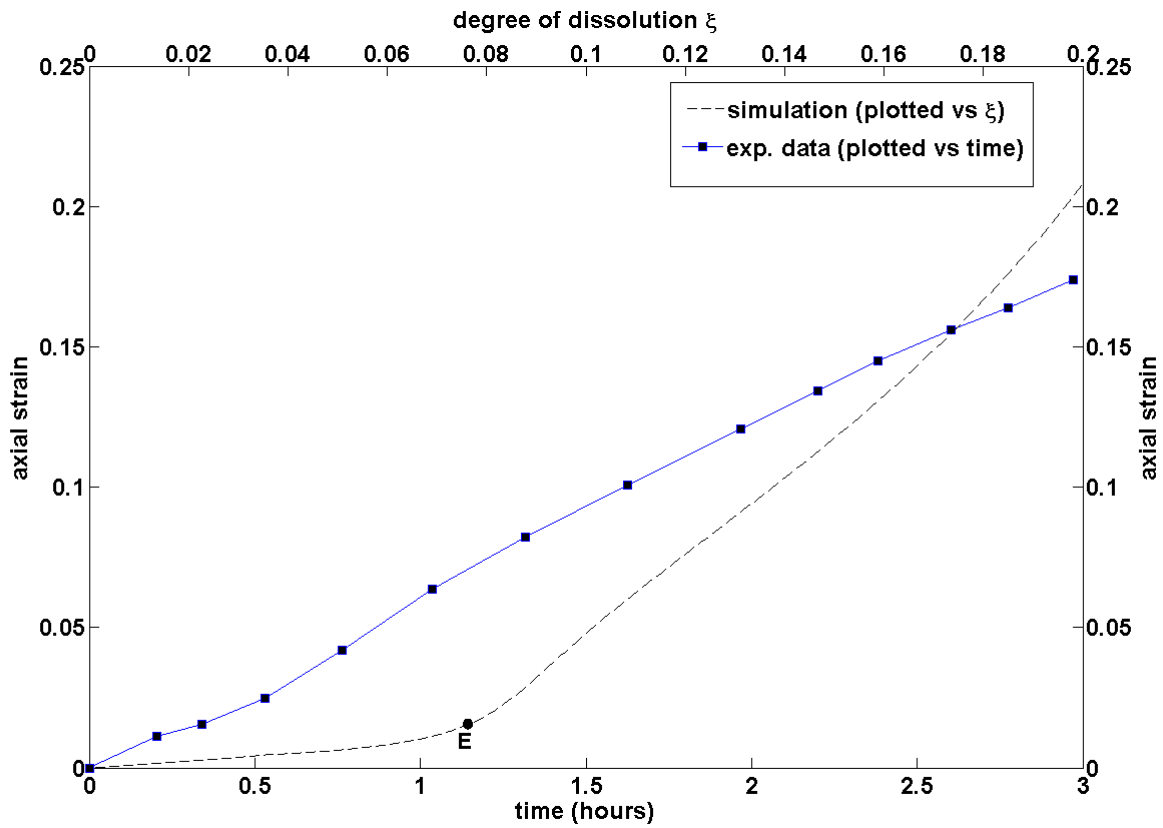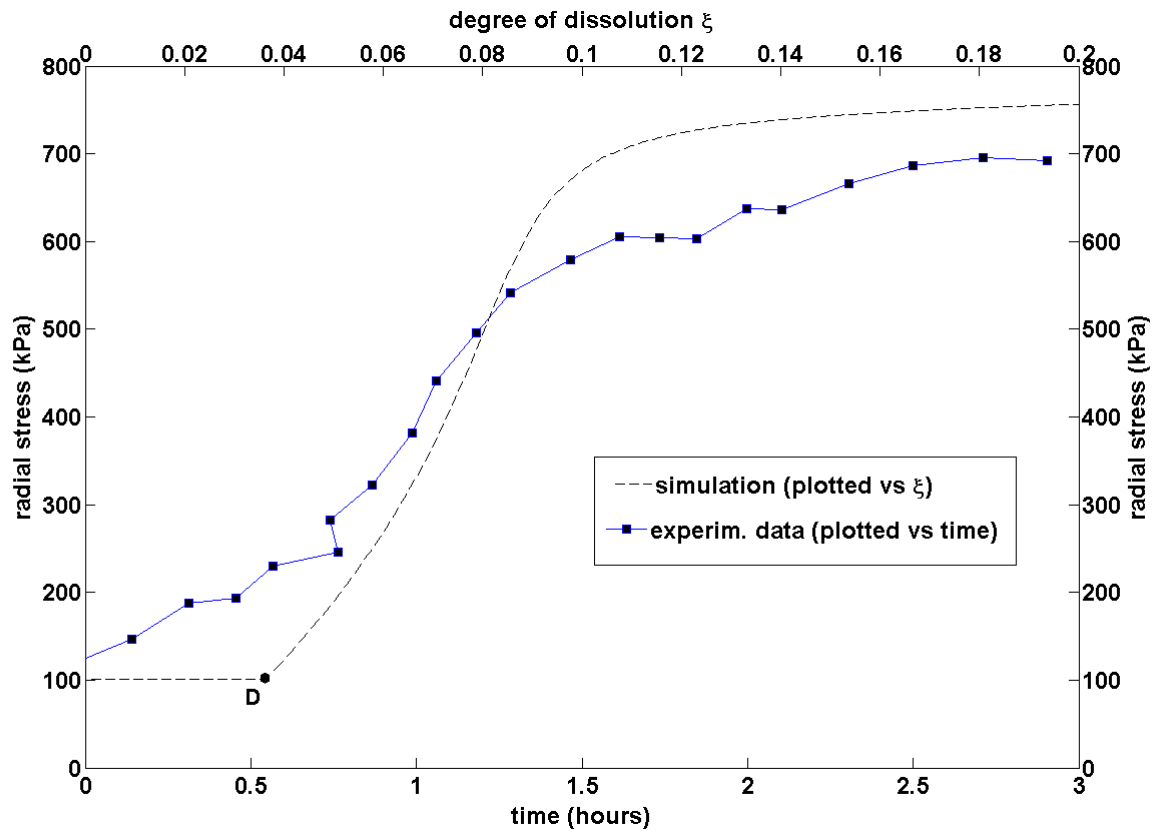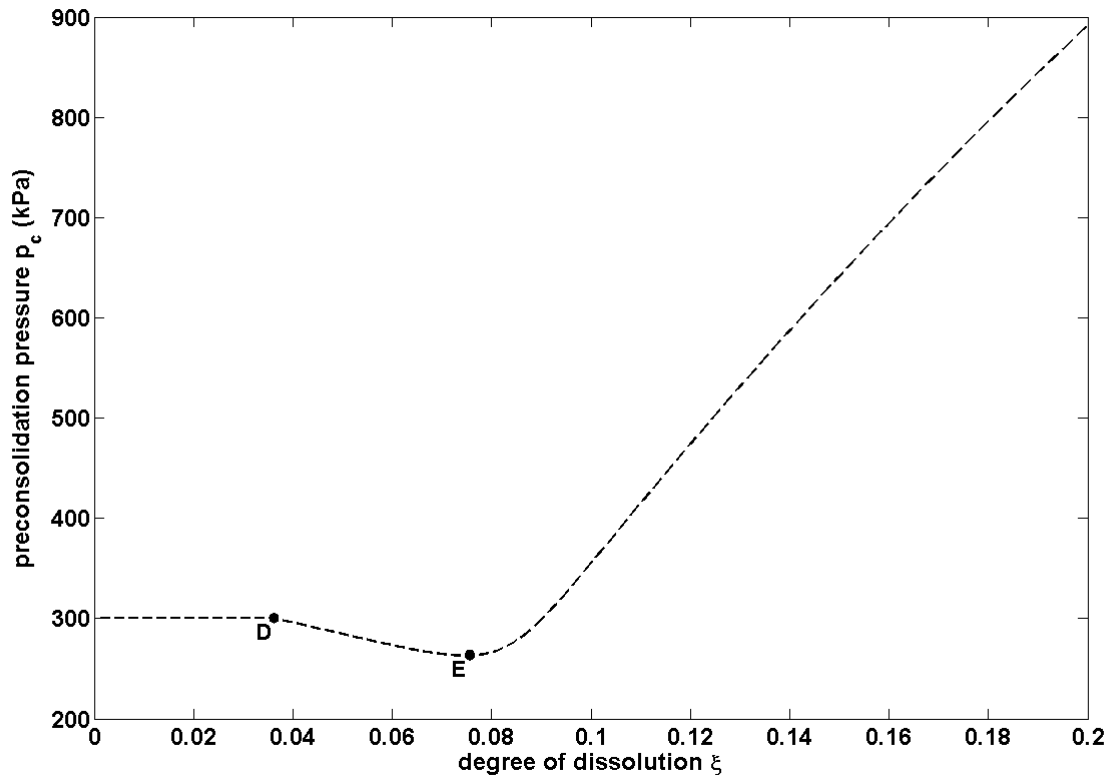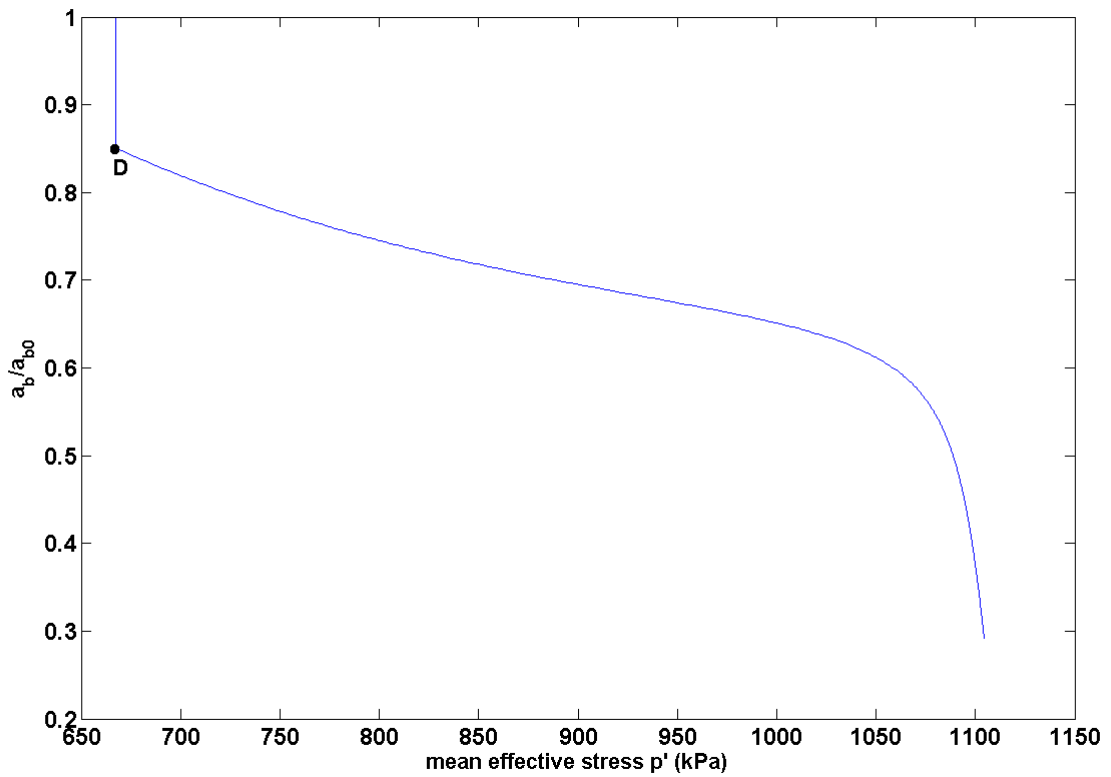
5

6

7

1

2

3 *Figure 12. Comparison of simulations and experimental data [30] in terms of (a) radial stress evolution and*

4 *(b) axial strain evolution, during the weathering phase at constant applied load in oedometric conditions.*

5 *The two datasets are not entirely comparable, since simulated values are plotted against the degree of*

1 *dissolution (upper horizontal axis), while the experimental data are reported as a function of time (lower*

2 *horizontal axis).*

3

1

2

3　*Figure 13. Simulated evolution of (a) preconsolidation pressure pc versus degree of dissolution, and (b)*

4　*normalized cross-sectional area of bonds against mean effective stress, during the weathering phase at*

5　*constant applied load in oedometric conditions. It should be noted that point D marks the onset of plastic*

1   *yield (cf. Figure12a), followed by an initial softening phase implying dilative behavior. Point E represents a*

2   *transition between dilative and contractive volumetric behavior (cf. Figure 12b), corresponding to zero*

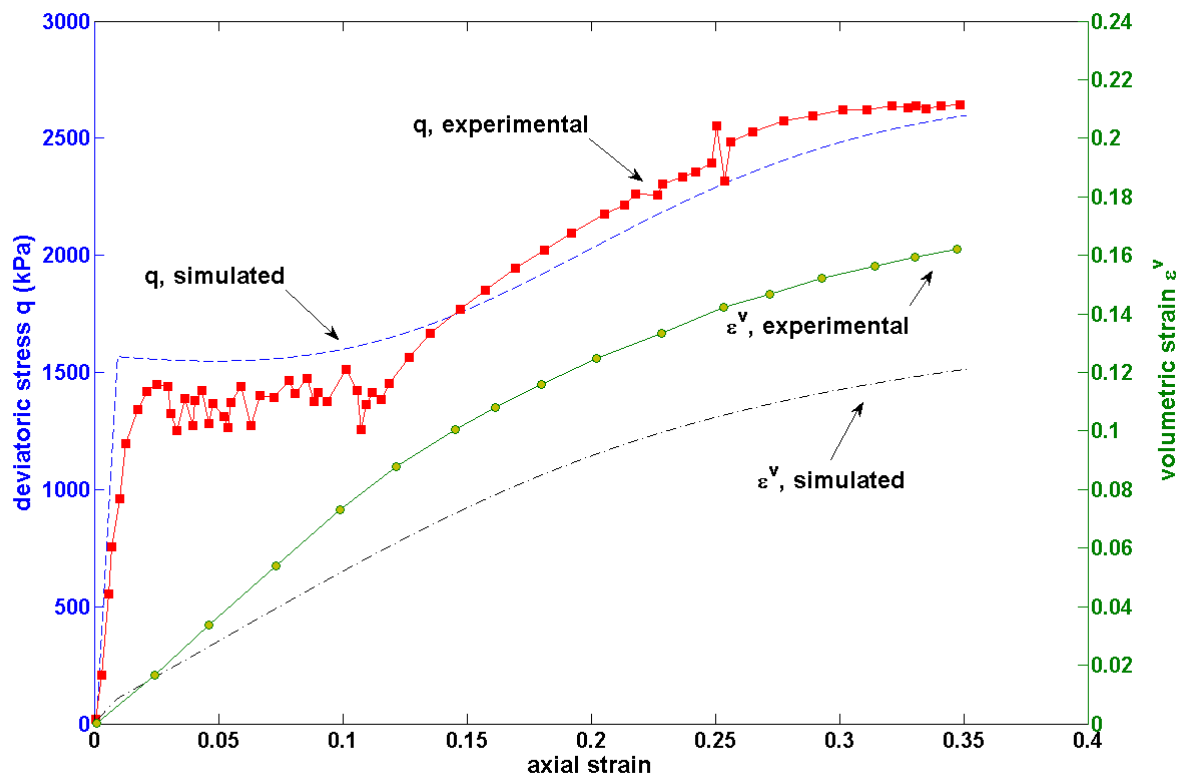3   *plastic volumetric strain rate.*

4

1
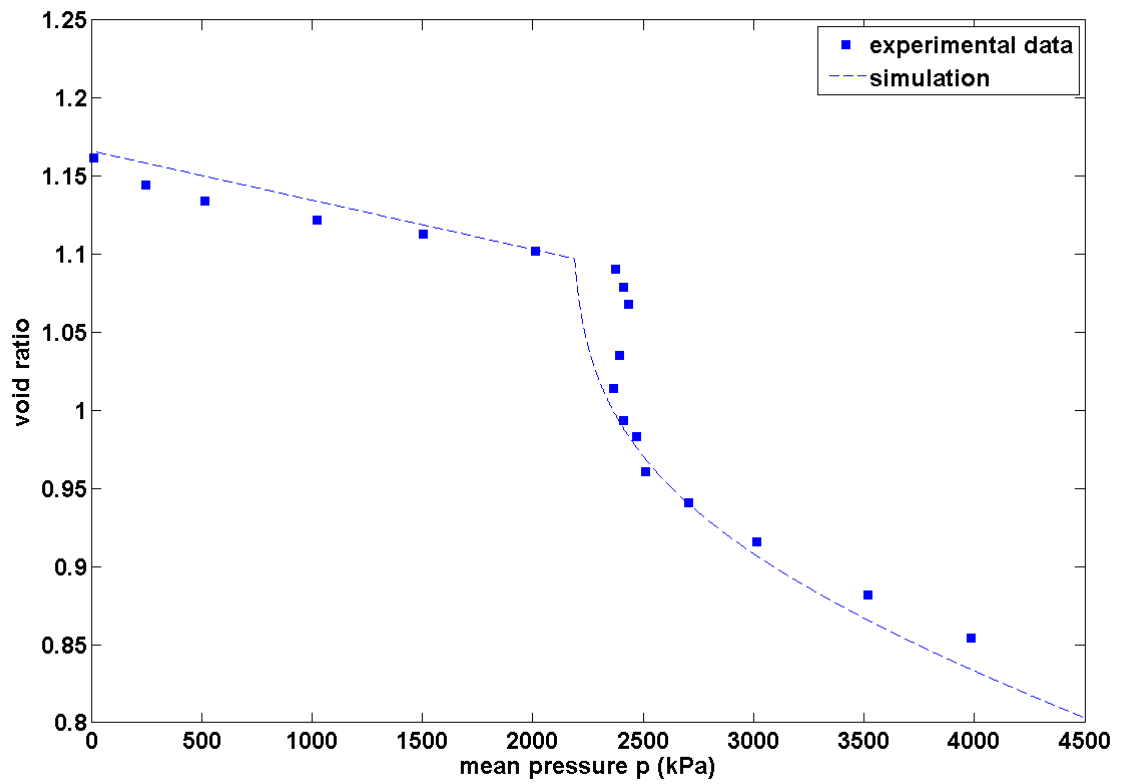
2

3   *Figure 14. Comparison of simulations and experimental data [36] in terms of axial strain versus axial*

4   *stress in a purely mechanical isotropic compression test on unweathered calcarenite.*

5

1
2 *Figure 15. Comparison of simulations and experimental data [36] in terms of deviatoric stress, and*
3 *volumetric strain, versus axial strain, in a purely mechanical drained triaxial compression test on*
4 *unweathered calcarenite.*

5

1 **List of Tables**

2 *Table 1. Parameter values adopted for model validation simulations.*

Parameter	Symbol	Set #1	Set #2	Units
Initial porosity	n_0	0.56	0.56	
Elastic modulus of uncemented solid skeleton	E_g	1	1	Mpa
Elastic modulus of cement material	E_b	150	150	Gpa
Poisson ratio of solid skeleton and bonds	v_g, v_b	0.053	0.053	
Critical state parameter	M_{cv}	1.51	1.15	
Initial mean radius of grains	R_g	0.05	0.05	mm
Initial mean radius of bond cross-sections	R_b	0.009	0.0105	mm
Mean bond length	d	0.008	0.008	mm
Destructuration plastic strain parameter	A	0.8	0.8	
Mechanical destructuration rate parameter	k_1	0.8	30	
Chemical healing rate parameter	k_2	0	0	m^3/kg
Slope of normal consolidation line	λ	0.05	0.025	
Number of grains	N_g	8.0×10^{11}	8.0×10^{11}	m^{-3}
Number of bonds	N_b	$= 11 \times N_g$	$= 11 \times N_g$	m^{-3}
Initial number of active bonds	N_{ba}	$= N_b$	$= N_b$	m^{-3}
Tensile strength of cement material	σ_{rt}	8	8	Mpa
Compressive strength of cement material	σ_{rc}	90	90	Mpa
Uncemented preconsolidation stress	p_c	300	50	kPa
Constitutive parameter	β	2	2	
Constitutive parameter	γ	0.67	0.67	
Constitutive parameter	δ	0.5	0.5	
Constitutive parameter	θ	3.5	3.5	
Constitutive parameter	a_{r0}	1	1	1/mm

3